공학박사학위논문

Segmented Piezoelectric Skin Energy Harvesters

분절된 스킨형 압전 에너지 수확장치

2014 년 8 월

서울대학교 대학원

기계항공공학부

김 홍 진

Abstract

Segmented Piezoelectric Skin Energy Harvesters

Kim, Hongjin

School of Mechanical and Aerospace Engineering

The Graduate School

Seoul National University

This work proposes segmented piezoelectric skin energy harvesters that work effectively at any operating vibration frequencies. Unlike earlier studies to make use of an analytical model for piezoelectric energy harvesting (PEH) skin design, this work proposes an experiment-based method to design a skin-based PEHs in which operating deflection shapes (ODSs) of a target mechanical system are utilized for the design. This method is practically useful because actual vibrations of a target mechanical system are fully considered in designing skin-type PEHs. In order to consider actual defection shapes of a target system, in-plane normal strain values are interpolated from discretely-measured out-of-plane deformations of a target mechanical system. Then, information on possibly-multiple strain inflection lines is extracted and segmented PEH skins are determined accordingly. This procedure is devised to avoid any adverse voltage cancellation which may take place if a skin is not segmented but used as a whole. For a test system considered in this study, which is an outdoor condensing unit of an air conditioner, the direct-type PEH skin is

preferred to be segmented into four pieces. The harvested energy is used to power a wireless sensor network. The experiments with and without the segmentation confirmed that the proposed segmentation scheme produces much larger electric output than a single-piece scheme.

As an extension of this approach, possibly useful in some hostile environments such as a target system having a curved surface or an available region of small in-plane strain, a modified method using "add-on" type PEH skins is also suggested. In this case, the ODS of a target mechanical system is considered to locate strain inflection lines by using finite element simulation. Unlike the direct-type PEH skin cases, finite element analysis can be effectively used for the add-on type PEH skin because the finite element modeling is rather simple and accurate. Also, the optimal sizes of PEH skin segments are determined to maximize the total power output. The method of using the proposed three add-on type PEH skin segments is experimentally validated. It is shown that this approach is effective especially when the output is rectified.

Key words: Energy harvesting, operating deflection shape, strain inflection line, wireless sensor.

Student Number: 2009-31245

Contents

List of Tables

List of Figures

vii

viii

ix

x

Chapter 1

Introductions

Energy harvesting from ambient sources has been recognized as a promising powering technology for portable or wireless electrical devices [1-10]. Among various types of energy sources, energy harvesting from mechanical vibration has received much attention, because of its promising power density and abundant presence around sensor locations. Four basic transduction mechanisms are used for vibration-to-electric energy conversion. They are electromagnetic induction [11-14], electrostatic [15-18], piezoelectric [19-22], and magnetostriction [23-25]. Among these mechanisms for converting ambient vibrations into electricity, piezoelectric transduction has received much attention, because of its promising power density and high energy conversion efficiency [26-30]. The piezoelectric energy harvesting (PEH) has been realized in various structural forms [31-37], one of which is a well-known simple cantilever type.

In the last two decades, researchers have investigated various problems related to modeling [38-44] and designing [45-48] the cantilever type PEH devices. A reliable mathematical modeling of the PEH device is very important in the sense that it allows

1

to identify the effects of design parameters and predict the electrical output, moreover, the PEH device can be optimized to have maximum electrical output for a given input. The modeling approaches in the literature include coupled single degree-of-freedom (SDOF) models (or so called the lumped parameter models) [7, 43, 44, 49-51], approximate distributed parameter models (the conventional combination of the variational principle and the Rayleigh-Ritz method based on the Euler-Bernoulli beam assumptions) [43, 52-54], and the continuous distributed parameter modeling approach [40, 42]. The design studies of cantilever type PEH are mainly conducted to enhance power output and expand operating frequency bandwidth. Some researchers have found that a trapezoidal shaped cantilever is more efficient than a rectangular shaped cantilever, since the strain distribution of the trapezoidal cantilever is uniformly large all over the beam surface [8, 45, 46]. Zheng et al. [47] and Kim et al. [55] have employed topology optimization technique for an optimal cantilever type PEH design by maximizing the energy conversion efficiency between mechanical and electric energy. To enhance the power generation capability, some researchers have employed permanent magnets as the tip mass of the cantilever [56-59]. In this way, the EH device can involve both piezoelectric and electromagnetic conversion mechanisms. To expand the operating frequency bandwidth of the cantilever type PEH, some researchers have used arrays of cantilevers having different resonant frequencies [60, 61]. The operating frequency bandwidth can be easily expanded by increasing the number of cantilevers, while this cannot contribute much to output power enhancement. Also, Challa et al. [62] reported a resonance frequency tunable PEH device. The attractive and repulsive force of permanent magnets are employed to modulate the resonance frequency of the PEH cantilever to match the source frequency.

2

Even though most PEH devices take form of a cantilever, cantilever type PEH has some limitations in the practical point of view. First, the cantilever type PEH device requires more space due to a bulky tip mass and additional clamping part. Second, it is suggested to keep the cantilever type PEH device (including the tip mass and the clamping part) inside a protection housing, since performance of the PEH device can be adversely affected by some environmental harm (such as dirt and moisture). Third, after a long-term exposure to vibration, clamping conditions of the cantilever type PEH device can become loosened. This results in a great loss of vibration energy otherwise converted into electric power. In order to overcome the above mentioned drawbacks of the cantilever type PEH, a skin-type piezoelectric energy harvester was also introduced by Lee and Youn [63, 64]. In the earlier works on the PEH skin design, a skin is formed with thin piezoelectric patches attached directly onto a vibrating shell structure, which can be found in various kinds of mechanical systems such as HVAC facilities, home appliances, vehicles, etc. The structure is considered as a substrate for thin piezoelectric patches. Directly attached to a target mechanical system, a PEH skin does not require an additional fixture unlike a cantilevered PEH device.

The voltage cancellation effect [33, 34, 48, 65, 66] should be taken into account for maximizing the harvested power. Should a single piezoelectric patch experience the voltage cancellation as shown in Figure 1.1, the generated power can be substantially reduced. Separation of one patch into multiple patches is thus inevitable for power maximization. So far two methods [65, 66] have been investigated to implement the piezoelectric patch separation lines along with: (a) voltage phase changes and (b) in-plane normal strain sign changes.

3
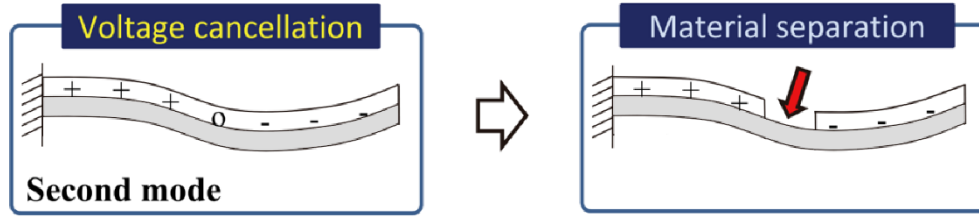
Fig. 1.1 Phenomenon of voltage cancellation on a cantilever in the secondary vibration mode and a material separation idea to eliminate the cancellation.

Lee and Youn [64] analytically addressed a multimodal PEH skin design by considering multiple harmonic vibration modes. The target mechanical system was modeled using a finite element method, and the boundary conditions were tried to be tuned considering vibration levels measured from a few points. However, this analytical approach to the PEH skin design is limitedly applicable because it is extremely difficult to precisely model the vibration response of an actual mechanical system. In this work, instead of applying the finite element analysis, experimentally measured ODSs of a target mechanical system are employed to find strain inflection lines for the direct-type PEH skin design.

The ODS is a very well-known technique to show the deflection of target structure at a particular frequency [67-70]. More generally, it is a technique to express forced motion of two or more points on a structure. Compared with a mode shape, the ODS contains both the forced and resonant vibration information of the structure, while the mode shape characterizes only the resonant vibration of the target structure. By using

4

the ODS, the actual motion of the mechanical system can be obtained. Moreover, the resonance frequency and mode shape can be identified from the ODS measurement. In fact, the ODS allows an easy and quick modal investigation, since it is accomplished by only measuring response of the structure subjected to unknown and unmeasured input force. For this purpose, the excitation force must be applied on a non-nodal line, near the resonance frequency (or a broadband excitation). In this work, the ODS is utilized to obtain actual out-of-plane deflection of the target mechanical system. Since the in-plane strain data is required to locate a strain inflection line, not the out-of-plane deflection data, the in-plane strain of the target surface is calculated from the second spatial differentials of the measured out-of-plane deflection [71, 72].

Multiple strain inflection lines found at specific excitation frequencies are used for the final design of a direct-type PEH skin to enhance the energy harvesting capability. The proposed design methodology was demonstrated on a flat surface of an outdoor condensing unit. The effectiveness of the direct-type PEH skin was verified using several experiments and the four PEH skin segments successfully generated sufficient power to operate five wireless sensors (four accelerometers and one temperature sensor).

In addition, this work proposes an add-on type PEH skin to scavenge vibration of the target mechanical system having no appropriate surface to apply the direct-type PEH skin. Unlike the direct-type PEH skin, the PZT area of the add-on type PEH skin is inherently limited. Therefore resonance frequency of the add-on type PEH skin device is tuned to match the dominant source frequency and amplify vibration amplitude. Here, experimentally measured ODS of the target mechanical system is used to identify actual excitation frequency and magnitude. Using the identified

5

excitation frequency and magnitude, finite element analysis is employed to locate the strain inflection lines and optimize size of the PEH skin segments to maximize the total power output. The use of finite element analysis in designing the add-on type PEH skin is meaningful in the sense that its boundary conditions are relatively very easy to predict. The effectiveness of the add-on type PEH skin was verified using several experiments and a significant power could be generated especially when the output is rectified.

Both the two different types of segmented piezoelectric skin energy harvesters proposed in this research utilize ODS of the target mechanical system to identify and adopt actual vibration characteristics of the target. The type of the PEH skin can be selected depending on shape condition of the vibrating target surface. Since the piezoelectric material is chosen to be the PZT, its extremely brittle nature has limited the PEH skin application to a flat surface only. So, the direct-type PEH skin is designed to be applied onto a flat and large surface having plenty of in-plane strain fluctuation. This direct-type PEH skin is very compact and does not require any extra space above the vibrating target surface. Also, since the direct-type PEH skin is not operated at resonance frequency, performance of the PEH skin is not affected by the environmental harm (such as dirt and moisture) while the output power per unit area could be somewhat low. In case of a non-flat and/or small surface application where not enough in-plane strain is existent, the add-on type PEH skin can be applied. Since the brittle PZT requires flat surface, a flat substrate is fixed to the target surface by multiple clamping structures for structural stability. By using the resonance effect, the output power per unit area is much higher than the direct-type PEH skin while the

6

protection from the environmental harm is required. Also, extra space above the target surface is inevitable in case of the add-on type PEH skin.

Chapter 2

Direct-type PEH skin design based on ODS

2.1 Chapter overview

In this chapter, ODS based design of the direct-type PEH skin is proposed. As mentioned, it is noted that a key step in the PEH skin design is to properly separate piezoelectric patches so as to minimize unwanted power loss due to the voltage cancellation effect. Among existing two methodologies (i.e. based on voltage phase change or in-plane normal strain sign change) to separate the piezoelectric patches, this work employs in-plane strain sign change method to design a direct-type PEH skin. Relying on rather an experimental approach than a simulation, it is nearly infeasible to identify strain inflection lines by output voltage phase [64], which cannot be measured prior to the skin segmentation. A theoretical background on the identification of strain inflection lines based on in-plane normal strains is below explained for clear understanding of the proposed experimental skin design [73]. After the theoretical clarification, an outdoor condensing unit is selected as a target mechanical system to apply and experimentally verify the proposed design method.

8

The vibration characteristics of the selected outdoor condensing unit are analyzed and a design process of the direct-type PEH skin is proposed to utilize the experimentally measured ODS. The proposed design methodology was demonstrated on a flat surface of an outdoor condensing unit. Finally, regarding the actual vibration characteristics of the target surface, multiple strain inflection lines found at specific excitation frequencies are used to draw a direct-type PEH skin design, to enhance the energy harvesting capability.

2.2 Theoretical background of the strain inflection line

In this work, the direct-type PEH skin is segmented by the strain inflection lines identified using the in-plane normal strain distributions that are calculated from the ODS data of a target mechanical system. To explain the relationship between in-plane normal strain and voltage generation in a piezoelectric material, three-dimensional form of the linear piezoelectric constitutive equations will be first examined.

The piezoelectric patch used in this work (Piezo Systems, Inc., PSI-5H4E) is a transversely isotropic material, poled along the thickness direction. To be in agreement with the IEEE Standard on Piezoelectricity [74], the plane of isotropy is defined as the 12-plane (or the xy-plane) and therefore the axis of symmetry lies along the 3-direction (or the z-direction) as shown in Figure 2.1. Four field variables
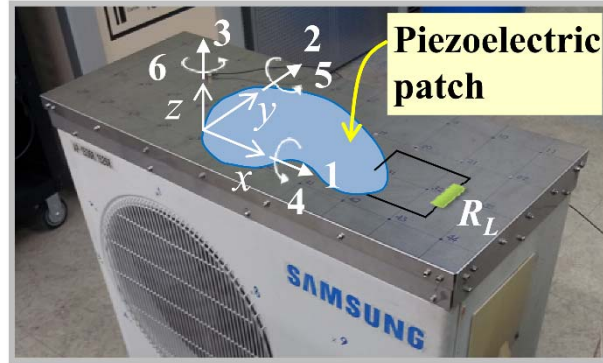
Fig. 2.1 Schematic of a direct-type PEH skin, attached onto a structure undergoing two dimensional surface strain fluctuations.

of the piezoelectric constitutive equations are the stress component (T_{ij}), strain components (S_{ij}), electric field components (E_k), and the electric displacement components (D_k).

The standard form of the piezoelectric constitutive equations can be given in four different forms by taking either two of the four above described field variables as the independent variables. These four different piezoelectric constitutive equation forms are represented as follows:

$$T_{ij} = c_{ijkl}^{E} S_{kl} - e_{kij} E_k \qquad (2.1a)$$

$$D_i = e_{ikl} S_{kl} + \varepsilon_{ik}^{S} E_k \qquad (2.1b)$$

and

$$S_{ij} = s_{ijkl}^{E} T_{kl} + d_{kij} E_k \qquad (2.2a)$$

$$D_i = d_{ikl} T_{kl} + \varepsilon_{ik}^{T} E_k \qquad (2.2b)$$

and

$$S_{ij} = s_{ijkl}^{D} T_{kl} + g_{kij} D_k \qquad (2.3a)$$

$$E_i = -g_{ikl} T_{kl} + \beta_{ik}^{T} D_k \qquad (2.3b)$$

and

11

$$T_{ij} = c_{ijkl}^D S_{kl} - h_{kij} D_k \tag{2.4a}$$

$$E_i = -h_{ikl} S_{kl} + \beta_{ik}^S D_k \tag{2.4b}$$

where e_{ikl}, d_{ikl}, g_{ikl}, and h_{ikl} are the piezoelectric constants, c_{ijkl}^E and c_{ijkl}^D are the elastic constants, and s_{ijkl}^E and s_{ijkl}^D are the elastic compliance constants. Also, ε_{ik}^S and ε_{ik}^T denote the permittivity constants while β_{ik}^S and β_{ik}^T stand for the impermittivity constants.

Among four different piezoelectric constitutive equation forms, consider the strain-electric displacement form (i.e., Equations (2.2a) and (2.2b)) where the independent variables are the stress components and the electric field components. This is a preferred form of the piezoelectric constitutive equations for bounded media (i.e., some of the stress components can be eliminated depending on geometry and/or some of the electric field components can be eliminated depending on the placement of the electrodes). Equations (2.2a) and (2.2b) can be given in matrix form as

$$\begin{bmatrix} \mathbf{S} \\ \mathbf{D} \end{bmatrix} = \begin{bmatrix} \mathbf{s}^E & \mathbf{d}^t \\ \mathbf{d} & \boldsymbol{\varepsilon}^T \end{bmatrix} \begin{bmatrix} \mathbf{T} \\ \mathbf{E} \end{bmatrix} \tag{2.5}$$

where the superscripts E and T denote that the respective constants are evaluated at constant electric field and constant stress, respectively, and the superscript t represents the transpose. The expanded form of Equation (2.5) is

12

$$
\begin{bmatrix} S_1 \\ S_2 \\ S_3 \\ S_4 \\ S_5 \\ S_6 \\ D_1 \\ D_2 \\ D_3 \end{bmatrix} = \begin{bmatrix} s_{11}^E & s_{12}^E & s_{13}^E & 0 & 0 & 0 & 0 & 0 & d_{31} \\ s_{12}^E & s_{11}^E & s_{13}^E & 0 & 0 & 0 & 0 & 0 & d_{31} \\ s_{13}^E & s_{13}^E & s_{33}^E & 0 & 0 & 0 & 0 & 0 & d_{33} \\ 0 & 0 & 0 & s_{55}^E & 0 & 0 & 0 & d_{15} & 0 \\ 0 & 0 & 0 & 0 & s_{55}^E & 0 & d_{15} & 0 & 0 \\ 0 & 0 & 0 & 0 & 0 & s_{66}^E & 0 & 0 & 0 \\ 0 & 0 & 0 & 0 & d_{15} & 0 & \varepsilon_{11}^T & 0 & 0 \\ 0 & 0 & 0 & d_{15} & 0 & 0 & 0 & \varepsilon_{11}^T & 0 \\ d_{31} & d_{31} & d_{33} & 0 & 0 & 0 & 0 & 0 & \varepsilon_{33}^T \end{bmatrix} \begin{bmatrix} T_1 \\ T_2 \\ T_3 \\ T_4 \\ T_5 \\ T_6 \\ E_1 \\ E_2 \\ E_3 \end{bmatrix} \tag{2.6}
$$

where the contracted notation (i.e., Voigt's notation: 11→1, 22→2, 33→3, 23→4, 13→5, and 12→6) is used for convenience. For Equation (2.6), note that the shear strain components in the contracted notation are the engineering shear strains (i.e., $S_4 = 2S_{23}$, $S_5 = 2S_{13}$, and $S_6 = 2S_{12}$).

Now, consider a piezoelectric patch attached to a thin substrate structure experiencing two-dimensional strain fluctuations. The structure can be modeled as a thin plane (i.e., Kirchhoff plate). According to this assumption, the normal stress in the thickness direction of the piezoelectric patch and the respective transverse shear stress components are negligible:

$$
T_3 = T_4 = T_5 = 0 \tag{2.7}
$$

Therefore, the Equation (2.6) is reduced as

$$
\begin{bmatrix} S_1 \\ S_2 \\ S_6 \\ D_3 \end{bmatrix} = \begin{bmatrix} s_{11}^E & s_{12}^E & 0 & d_{31} \\ s_{12}^E & s_{11}^E & 0 & d_{31} \\ 0 & 0 & s_{66}^E & 0 \\ d_{31} & d_{31} & 0 & \varepsilon_{33}^T \end{bmatrix} \begin{bmatrix} T_1 \\ T_2 \\ T_6 \\ E_3 \end{bmatrix} \tag{2.8}
$$

13

which can be rearranged to give

$$
\begin{bmatrix}
s_{11}^E & s_{12}^E & 0 & 0 \\
s_{12}^E & s_{11}^E & 0 & 0 \\
0 & 0 & s_{66}^E & 0 \\
-d_{31} & -d_{31} & 0 & 1
\end{bmatrix}
\begin{bmatrix}
T_1 \\ T_2 \\ T_6 \\ D_3
\end{bmatrix}
=
\begin{bmatrix}
1 & 0 & 0 & -d_{31} \\
0 & 1 & 0 & -d_{31} \\
0 & 0 & 1 & 0 \\
0 & 0 & 0 & \varepsilon_{33}^T
\end{bmatrix}
\begin{bmatrix}
S_1 \\ S_2 \\ S_6 \\ E_3
\end{bmatrix}
\tag{2.9}
$$

The stress-electric displacement form of the reduced constitutive equations become

$$
\begin{bmatrix}
T_1 \\ T_2 \\ T_6 \\ D_3
\end{bmatrix}
=
\begin{bmatrix}
\overline{c}_{11}^E & \overline{c}_{12}^E & 0 & -\overline{e}_{31} \\
\overline{c}_{12}^E & \overline{c}_{11}^E & 0 & -\overline{e}_{31} \\
0 & 0 & \overline{c}_{66}^E & 0 \\
\overline{e}_{31} & \overline{e}_{31} & 0 & \overline{\varepsilon}_{33}^S
\end{bmatrix}
\begin{bmatrix}
S_1 \\ S_2 \\ S_6 \\ E_3
\end{bmatrix}
\tag{2.10}
$$

where

$$
\overline{\mathbf{C}} =
\begin{bmatrix}
\overline{c}_{11}^E & \overline{c}_{12}^E & 0 & -\overline{e}_{31} \\
\overline{c}_{12}^E & \overline{c}_{11}^E & 0 & -\overline{e}_{31} \\
0 & 0 & \overline{c}_{66}^E & 0 \\
\overline{e}_{31} & \overline{e}_{31} & 0 & \overline{\varepsilon}_{33}^S
\end{bmatrix}
=
\begin{bmatrix}
s_{11}^E & s_{12}^E & 0 & 0 \\
s_{12}^E & s_{11}^E & 0 & 0 \\
0 & 0 & s_{66}^E & 0 \\
-d_{31} & -d_{31} & 0 & 1
\end{bmatrix}^{-1}
\begin{bmatrix}
1 & 0 & 0 & -d_{31} \\
0 & 1 & 0 & -d_{31} \\
0 & 0 & 1 & 0 \\
0 & 0 & 0 & \varepsilon_{33}^T
\end{bmatrix}
\tag{2.11}
$$

Here, the reduced elastic, piezoelectric, and permittivity constants are

$$
\overline{c}_{11}^E = \frac{s_{11}^E}{\left(s_{11}^E + s_{12}^E\right)\left(s_{11}^E - s_{12}^E\right)}
\tag{2.12}
$$

$$
\overline{c}_{12}^E = \frac{-s_{12}^E}{\left(s_{11}^E + s_{12}^E\right)\left(s_{11}^E - s_{12}^E\right)}
\tag{2.13}
$$

14

$$\overline{c}_{66}^{E} = \frac{1}{s_{66}^{E}} \tag{2.14}$$

$$\overline{e}_{31} = \frac{d_{31}}{s_{11}^{E} + s_{12}^{E}} \tag{2.15}$$

$$\overline{\varepsilon}_{33}^{S} = \overline{\varepsilon}_{33}^{T} - \frac{2d_{31}^{2}}{s_{11}^{E} + s_{12}^{E}} \tag{2.16}$$

Next, consider a piezoelectric patch with an external load resistance (R_L) as shown in Figure 2.1. The integral form of the Gauss's law for a dielectric material can be expressed as

$$\frac{\mathrm{d}}{\mathrm{d}t}\left(\int_{A} \mathbf{D} \cdot \mathbf{n} \mathrm{d}A\right) = \frac{v(t)}{R_{L}} \tag{2.17}$$

where $\mathbf{D}$ is the electric displacement vector, $\mathbf{n}$ is the unit outward normal vector, A is the electrode area of a piezoelectric patch, and $v(t)$ denotes the voltage across the external load resistance R_L.

From above Equation (2.10), the electric displacement of a thin piezoelectric patch undergoing the in-plane strain fluctuations in the xy-plane is expressed as

$$D_{3} = \overline{e}_{31}S_{1} + \overline{e}_{32}S_{2} + \overline{\varepsilon}_{33}^{S}E_{3} = \overline{e}_{31}\left(S_{1} + S_{2}\right) + \overline{\varepsilon}_{33}^{S}E_{3} \tag{2.18}$$

where S_1 and S_2 are the in-plane normal strain components, E_3 is the electric field intensity in the thickness direction, $\overline{e}_{31}$ and $\overline{e}_{32}$ are the piezoelectric stress

15

constants, and $\overline{\varepsilon}_{33}^S$ denotes the dielectric permittivity at constant strain. The over-bar denotes reduced quantities resulting from neglecting the transverse shear and thickness stress components, considering the transversely isotropy of piezoelectric material such as PZT. The reduced piezoelectric stress constants and dielectric permittivity can be respectively obtained as

$$\overline{e}_{31} = \overline{e}_{32} = \frac{d_{31}}{s_{11}^E + s_{12}^E} \tag{2.19a}$$

$$\overline{\varepsilon}_{33}^S = \varepsilon_{33}^T - \frac{2d_{31}^2}{s_{11}^E + s_{12}^E} \tag{2.19b}$$

where s_{11}^E and s_{12}^E are the elastic compliance at constant electric field, d_{31} denotes the piezoelectric strain constant, and ε_{33}^T denotes the dielectric permittivity at constant stress.

For more useful form of Equation (2.17), if the only nonzero electric displacement component shown in Equation (2.18) is substituted into Equation (2.17) and the electric field intensity is expressed in terms of the voltage across the external load resistance (R_L), Equation (2.17) leads to

$$\frac{\mathrm{d}v(t)}{\mathrm{d}t} + \frac{v(t)}{R_L C_p} = \frac{\overline{e}_{31}}{C_p} \int_A \frac{\partial}{\partial t}\left[S_1(x,y,t) + S_2(x,y,t)\right]\mathrm{d}A \tag{2.20}$$

where $C_p = \overline{\varepsilon}_{33}^S A / h_p$ is the capacitance of a piezoelectric patch and h_p is the thickness of a piezoelectric patch. Therefore, the voltage response is obtained from Equation (2.20) as follows:

16

$$v(t) = \frac{\overline{e}_{31}}{C_p} e^{\frac{-t}{\tau}} \int e^{\frac{t}{\tau}} \left\{ \int_A \frac{\partial}{\partial t} \left[S_1(x, y, t) + S_2(x, y, t) \right] dA \right\} dt \qquad (2.21)$$

From the equation above, it is obvious that the output voltage of a PEH skin is directly related to the sum of two in-plane normal strain components.

In this point, it is worth checking the directions of principal strain components and the way they change in time. Schematic of a rectangular rosette strain gauge having 45° angle between the gauges is shown in Figure 2.2. In general, at least three independent strain values are required to define a two-dimensional state of strain if no other information is provided. The rectangular rosette shown in Figure 2.2 gives three simultaneous strain measurements in A, B, and C-directions (i. e., S_A, S_B, and S_C, respectively). The directions of principal strain components S_1 and S_2 are denoted by 1 and 2.

Based on Mohr's circle [75], the principal strain components are obtained from the following strain transformation:

$$S_1 = \frac{S_A + S_C}{2} + \frac{1}{\sqrt{2}} \sqrt{(S_A - S_B)^2 + (S_B - S_C)^2} \qquad (2.22a)$$

$$S_2 = \frac{S_A + S_C}{2} - \frac{1}{\sqrt{2}} \sqrt{(S_A - S_B)^2 + (S_B - S_C)^2} \qquad (2.22b)$$

and the angle between gauge A and the direction of positive S_1 is

$$\theta = \frac{1}{2} \tan^{-1} \left(\frac{S_A - 2S_B + S_C}{S_A - S_C} \right) \qquad (2.23)$$

17

From Equations (2.22a) and (2.22b), note that

$$S_1 + S_2 = \frac{S_A + S_C}{2} + \frac{S_A + S_C}{2} = S_A + S_C \qquad (2.24)$$

which implies that the strain resultant of two arbitrary but orthogonal directions (i.e., $S_A + S_C$) is equal to that of the principal strain directions (i.e., $S_1 + S_2$). Although three independent strain values are required to determine the two-dimensional strain state of the surface, two orthogonal strain values are sufficient to estimate the resultant of the principal strain components. So, to locate strain inflection lines based on in-plane normal strain data of the target surface, direction of the two strains can be arbitrarily selected only if the two strain components are orthogonal to each other.

By the way, in general a piezoelectric skin (0.127 ~ 0.267 mm) is much thinner than a vibrating substrate structure (1.0 ~ 3.0 mm). Also, it is assumed to have a perfect bonding between the skin and the shell structure in this study. It is thus reasonable to say that the average strain distribution of the PEH skin is similar to that of the substrate structure. In the proposed PEH skin design, therefore, the criteria to properly determine strain inflection lines is simply to identify the locations on the substrate structure, at which the sum of two in-plane normal strain components becomes zero, i.e., $S_{sum} = S_1 + S_2 = 0$.
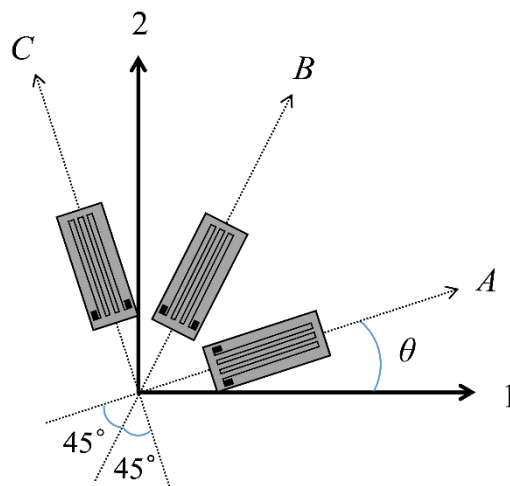
Fig. 2.2 Schematic of a rectangular rosette configuration with gauges in A, B, and C-directions, and the principal strain directions 1 and 2.

2.3 Target selection and vibration characterization

2.3.1 Target selection and modifications

The proposed design method enhances a practical aspect of the PEH skin so that it can be applied to operating plant facilities. Prior to such a practical application, an in-lab facility was devised to clearly validate the proposed idea and realize potential challenges in a practical situation. Unlike most experimental validation works executed with an ideal structure and an electromagnetic shaker, this work employed the outdoor condensing unit of an air conditioner as a target mechanical system as shown in Figure 2.3(a). Given harmonic vibrations produced by an electromagnetic motor of the cooling fan inside (Sungsin Co., IC-9630SLF6E; operating at 1170 ~ 1180 rpm), the outdoor condensing unit with a large top plate ($800 \times 300 \times 1$ mm^3) is very appropriate for the demonstration study of the direct-type PEH skin design.

The vibration characteristics of the top plate is examined. The maximum vibration on the top plate transmitted from a cooling fan inside was measured at the level of $0.1 \sim 0.2$ g (1 g = 9.8 m/s^2). This vibration level was relatively low in comparison with that found in actual plant facilities, which was in the range of $2 \sim 3$ g (measured from a fan blower unit in the 1st power plant, Seoul National University Gwanak Campus). So, the amount of vibration is increased to the level found in plant facilities by adding a small degree of eccentricity to the fan rotation. After this improvement, the vibration level of the top plate is reexamined. The vibration level was enhanced, but it is found that the characteristics results were not reproducible as shown in Figure 2.3(b) and (c). This was mainly due to mixed and heavily random boundary conditions. While rigidly constrained by two side walls, the plate was loosely

20
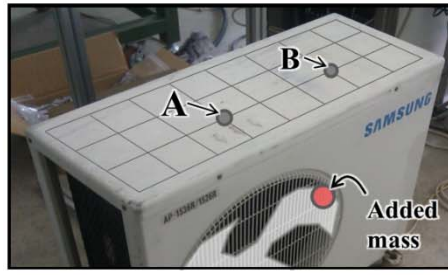
(a)
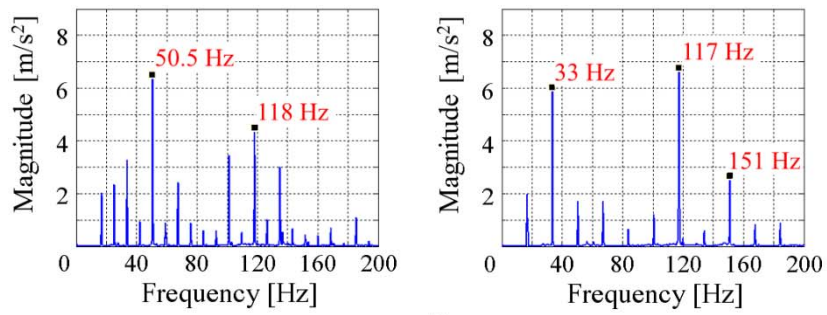
(b)
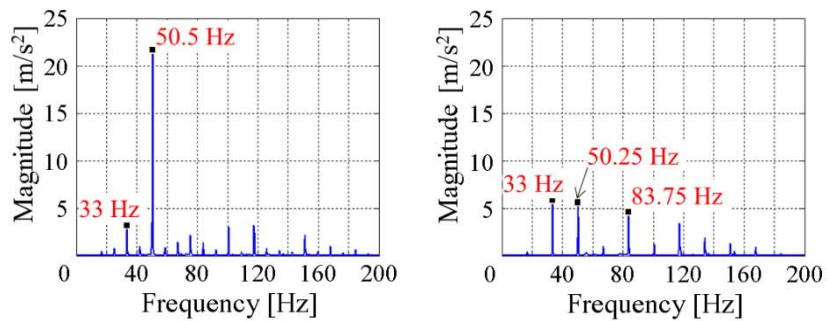
(c)

Fig. 2.3 (a) The original top plate of the outdoor condensing unit examined with a mass added to one of the three blades in a cooling fan. Fast Fourier transformed results of vibration measured at two different time (b) from grid point A and (c) from grid point B, showing no reproducibility.

constrained by two other side walls and upheld at the center by an inner vertical supporter. Especially, the inner supporter was considered to be the main cause of this randomness, since it was loosely upholding the top plate without any solid fixing (see Figure 2.4(a)).

Therefore, as shown in Figure 2.4(b), the outdoor condensing unit was modified to enhance the measurement reproducibility by minimizing the randomness in the boundary conditions, along with the increased amount of vibration level. The modification was thus done in three-fold by: (a) adding a mass of 20 gram to one of the three blades in a cooling fan to enhance the excitation vibration level, (b) extending heights of the side walls so that the inner vertical supporter cannot interfere the top plate, and (c) replacing the top plate having flat surface without any embossed region. In summary, the top plate becomes clamped along the sides only (i.e., no upholding inner supporters at the middle of the plate) with increased vibration level through the modification.
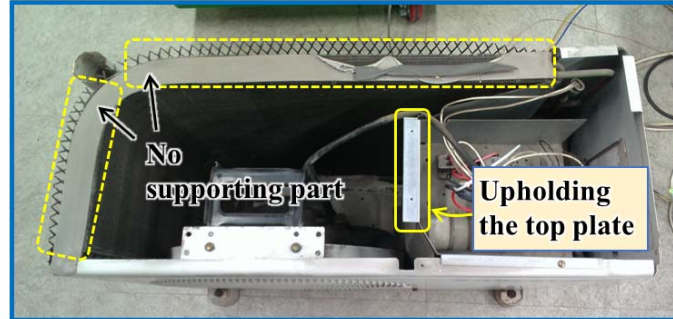
(a)
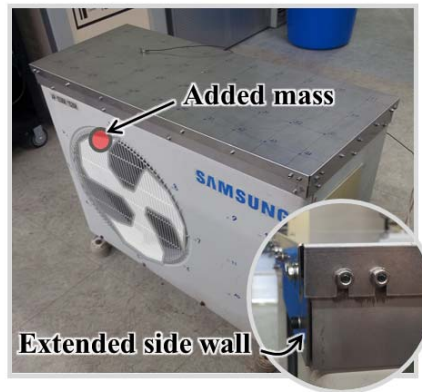
(b)

Fig. 2.4 (a) Structure inside the outdoor condensing unit with mixed and heavily random constraints of the top plate and (b) modification of the condensing unit with extended side walls and an added mass.

2.3.2 Vibration characterization

After the modifications, the vibration characteristics of the top plate was again measured and characterized. This characterization process, to be of great essence for a successful PEH skin design, employs two measurement techniques: modal testing and ODS characterization.

First, modal testing by an impact hammer (PCB Piezotronics, Inc., 086C03) and an accelerometer (Brüel & Kjær, Type 4394) was performed to examine vibration characteristics of the top plate at 11×5 grid points [76]. In the testing, the accelerometer was fixed near a grid location (i.e., near the grid point (4,4) regarding the front left corner of the top plate as the origin) and the impact hammer was moved along the 55 grid points to examine the mode shape of the top plate. The result of the modal testing proves that the modified top plate has reproducible vibration characteristics. A frequency response function result of a certain grid point is shown in Figure 2.5(a). The first three resonance frequencies are found to be 32.7, 48.3, and 69.9 Hz. Also, three mode shape results of the top plate corresponding to these three resonance frequencies can be found in Figure 2.5(b). The resonance frequencies are very difficult to predict by simulation (such as finite element analysis) unless well-tuned boundary conditions are used. While the tuning itself poses much challenge, the simplified analysis with ideal fully-clamped boundary conditions predicts the resonance frequencies of 97.7, 116.8, and 151.9 Hz, which are far off from the experimental results. This discrepancy highlights the importance of this experimental method because it is free from the prediction error in the analytical approach. Later this discrepancy is found to be mainly due to the unacknowledged modeling errors in boundary conditions and material modeling.

24
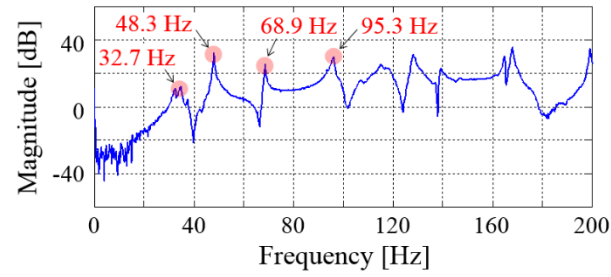
(a)
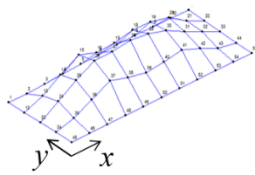
1st mode: **32.7** [Hz]   **2**nd mode: **48.3** [Hz]   **3**rd mode: **68.9** [Hz]
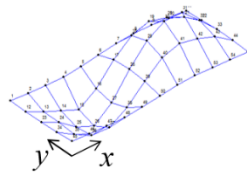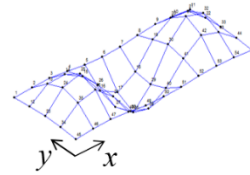
(b)

Fig. 2.5 Identified inherent vibration characteristics of the outdoor condensing unit's top plate: (a) a frequency response function result to indicate resonance frequencies and (b) mode shapes at the first three resonance frequencies.

25

Then, the ODS characteristics of the top plate were examined to check a vibration response in the presence of actual excitation and select the frequencies of interest. Known as the driving frequency of 19 ~ 20 Hz induced by the fan rotation (1170 ~ 1180 rpm), the lowest peak frequency measured on the top plate was around 18 Hz prior to the modification but slightly lowered to 16 ~ 17 Hz after the modification. The eccentricity by the added mass has interfered the fan rotation, resulting in a slightly lowered driving frequency. Taking this as a base frequency, the top plate was excited at its harmonics as shown in Figure 2.6(a). The ODS results are shown in Figure 2.6(b). In this work, a scanning laser vibrometer (Polytec Gmbh., PSV-400) was used to measure the ODS of the top plate at 25×11 grid points. Three meaningful deflection shapes having large deformation were found at 33.8, 50.0, and 66.9 Hz and the corresponding peak acceleration levels were measured as 2.8, 2.4, and 0.9 g, respectively. It is noted that three frequencies measured are near the harmonics of the first peak frequency (16 ~ 17 Hz) by the cooling fan. Moreover, as compared in Figure 2.5(b) and 2.6(b), the ODS and modal testing results look very similar. This could happen because these three frequencies are near the resonance frequencies of the top plate by accident.

(a)

1st harmonic: **33.8** [Hz]   2nd harmonic: **50.0** [Hz]   3rd harmonic: **66.9** [Hz]

Max 2.8 [g-level]   Max 2.4 [g-level]   Max 0.9 [g-level]
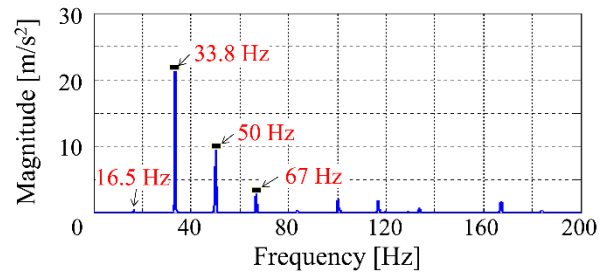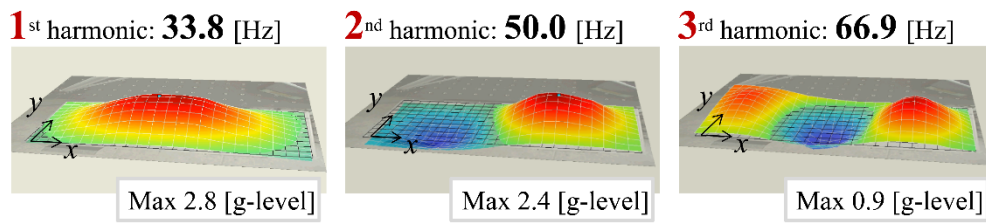
(b)

Fig. 2.6 Identified vibration characteristics of the outdoor condensing unit's top plate under operation: (a) a fast Fourier transformed result to indicate excitation frequencies and (b) three operating deflection shapes at frequencies of interest.

27

2.4 Design process for the outdoor condensing unit

Designing a direct-type PEH skin requires, two in-plane normal strain components (S_{sum}) to locate the strain inflection lines. It is impossible to measure the in-plane normal strains over a large area. This work instead measures the out-of-plane deflection (i.e., the ODS) of a target mechanical system and then calculated the in-plane normal strain components to locate strain inflection lines [71, 72]. Following six design steps are proposed, and they are applied to design a direct-type PEH skin for the top surface of outdoor condensing unit.

Step 1: Select a target mechanical system and determine grid information (i.e., size, number of grid points, etc.) considering size of the target mechanical system and vibration mode. In this work, top plate of the outdoor condensing unit is selected to apply proposed design method of the direct-type PEH skin. The size of the top plate was measured to be 800×300 mm^2, and divided into 25×11 grid points to have nearly square-shaped grids of 32.3×30.5 mm^2, as shown in Figure 2.7.

Step 2: Measure ODS and determine frequency ranges of interest having meaningful deflection shapes. Acquire the out-of-plane deflection data of the target mechanical system at the frequencies of interest. The ODS of the top plate was measured using a scanning laser vibrometer (Polytec Gmbh., PSV-400). Three meaningful deflection shapes were found at 33.8, 50.0, and 66.9 Hz (see Figure 2.6(b)), and therefore a total of 275 out-of-plane-deflection data can be acquired from every grid points for each frequencies.

28
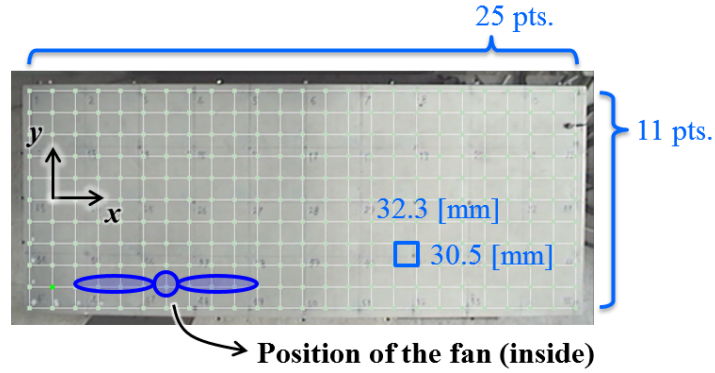
Fig. 2.7 Grids on the top plate of the outdoor condensing unit to measure the ODS and approximate location of the vibration source.

Step 3: Represent the out-of-plane deflection data using polynomial curve fitting. To replicate the deformed shape of the top plate, continuous out-of-plane deflection data are required. For a frequency of interest (say, 33.8 Hz), the 275 data obtained above were employed for the polynomial curve fitting of the out-of-plane deflection. Before polynomial curve fitting, these data must be grouped in datasets along the grid lines. Along 11 grid lines in the x-direction, 11 datasets each having 25 values can be obtained. Likewise, 25 datasets each having 11 values are obtained in the y-direction. Then, MATLAB was used to approximate the datasets with 4 to 8th-order polynomials, which could best replicate the ODS of the top plate. The polynomials had the acceptable R-squared values of 0.990 and 0.970 in the x- and y- direction,

respectively. As a result, the ODS of the top plate at a frequency of interest is expressed with 36 piecewise polynomials.

Step 4: Calculate the sum of the in-plane normal strain from the fitted out-of-plane deflection, using the following Equation (see Stanbridge et al. [71]) as:

$$S_{sum} = S_1 + S_2 = \frac{h}{2}\left(\frac{\partial^2 w}{\partial x^2} + \frac{\partial^2 w}{\partial y^2}\right) \tag{2.25}$$

where h and w represent the plate thickness and the out-of-plane deflection, respectively.

Step 5: Draw the strain distributions using the calculated in-plane normal strain values over the target surface and locate the zeroes of S_{sum} for the strain inflection lines. Figure 2.8 illustrates three strain inflection lines for three frequency values (33.8, 50.0, and 66.9 Hz) defined as the minimum of the absolute values of S_{sum}.

Step 6: Determine the number of the strain inflection lines of which the harmonics are included in the frequency ranges of interest. Three strain inflection lines were considered in the final design, because the 4th harmonic showed less than 7 % deformation compared with the 1st harmonic deflection. Figure 2.9 shows the segmented design of the PEH skin. The design was obtained by superposing the strain inflection lines in the three harmonics while taking into account the manufacturability. In the superposition, a higher weight is applied to a lower frequency mode because the lower mode produces much energy in general.

30
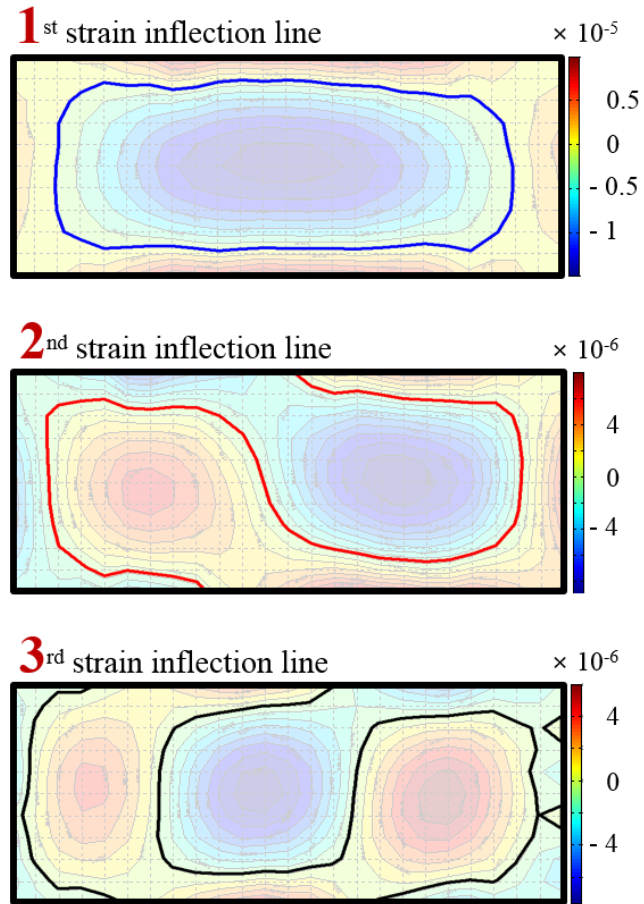
Fig. 2.8 The strain distribution results and corresponding strain inflection lines of the direct-type PEH skin, at three frequencies of interest values (i.e., 33.8, 50.0, and 66.9 Hz).
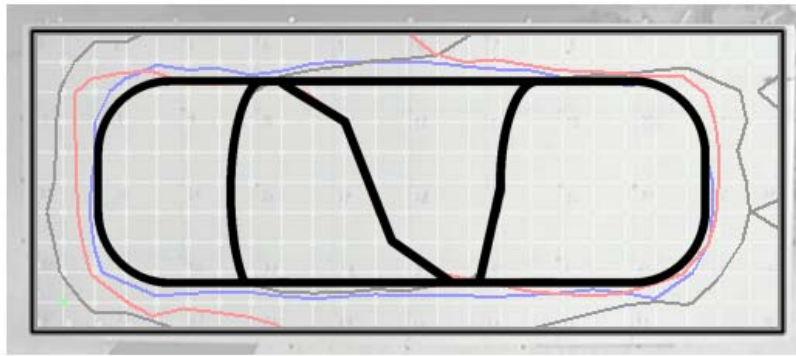
Fig. 2.9 The proposed design of the direct-type PEH skin obtained by superposition of three strain inflection lines.

Chapter 3

Direct-type PEH skin fabrication and its experimental validation

3.1 Chapter overview

In this chapter, previously proposed design of the direct-type PEH skin is fabricated. The most important component of a PEH will be the piezoelectric patch. Among various materials having piezoelectricity, the PZT (Lead Zirconate Titanate) is selected as the piezoelectric material for its high piezoelectric coefficients. Though the PZT is one of the most commonly used engineering piezoceramics due to its high energy conversion efficiency, it is sometimes very difficult to handle this material because of the very brittle nature. Especially it is very difficult to cut PZT sheets (Piezo Systems, Inc., PSI-5H4E) into a desired shape, if the design includes curved edges. In this work, a CNC laser cutter (Universal Laser Systems, Inc., M-300 Laser Platform) is used to cut PZT sheets as designed. Including the CNC cutting process, a fabrication process of the direct-type PEH skin is proposed and will be discuss in the next section. Also, the effectiveness of the direct-type PEH skin is validated using several experiments.

3.2 Fabrication process of a direct-type PEH skin

As can be seen in Chapter 2, the proposed design of the direct-type PEH skin includes a lot of curved edges. To realize this design, one of the most challenging part of the PEH skin fabrication is the PZT cutting, since the PZT sheets are extremely brittle. In this work, a CNC laser cutter is employed to cut PZT sheets into exactly desired shapes. The following steps are proposed to fabricate the direct-type PEH skin, and this process is also illustrated in Figure 3.1.

Step 1: Prepare a two-dimensional CAD file of the skin design in an actual size using a drawing software such as AutoCAD. This CAD file is necessary not only to use the CNC laser cutter, but also to sketch the exact location of PEH skin segments on the target surface.

Step 2: Load the CAD file to the CNC laser cutter and cut PZT sheets using the laser cutter. Since the size of proposed direct-type PEH skin design is much larger than a single PZT sheet (72.4 mm square sized), each PEH skin segment must be composed of multiple PZT sheets. In this step, therefore, it is very important to make sure that the poling direction of the PZT sheets are aligned consistently, as shown in Figure 3.1.

Step 3: Sketch the PEH skin design on the top plate surface of outdoor condensing unit to locate the piezoelectric patches machined in Step 2. To find exact location of the PEH skin segments, actual sized hard copy of above prepared CAD file is very useful, because the size of this hard copy exactly matches the design area of target surface.

34

Step 4: Attach the laser-machined PZT sheets to the top plate using a conductive epoxy (ITW Chemtronics, CW-2400). Make sure to deploy the PZT sheets consistently, to have the poling direction aligned. Also, the conductive epoxy should be evenly spread on the target surface. In this step, it is very difficult to control proper amount of the conductive epoxy, which is easily overflowed. Moreover, since the PZT sheets are very thin (0.267 mm), overflowed conductive epoxy frequently reaches the top surface of the PZT, which causes an electric short. Therefore, every side edges of the laser-machined PZT sheets are coated with enamel. In this way, little overflowed conductive epoxy can be blocked to reach the top electrode of PZT sheet.

Step 5: Check if any PZT sheet is electrically short or not. Redo Step 4 for the PZT sheets identified to be in electrically short state.

Step 6: Cure the epoxy for 6 hours at room temperature with a uniformly distributed weight of around 2 kg on the PZT sheets. This curing step is very important since the thickness of the conductive epoxy can be uniformly adjusted, and therefore, the PZT sheets are firmly bonded to the substrate structure through this process. After the curing process is over, some retouch might be required on PZT sheets, which are newly discovered to be electrically short.

Step 7: Connect the PZT sheets in one PEH skin segment using an electric tape. Now, the PZT sheets in each PEH segments share the equipotential surface, and therefore can be treated as a single unit.
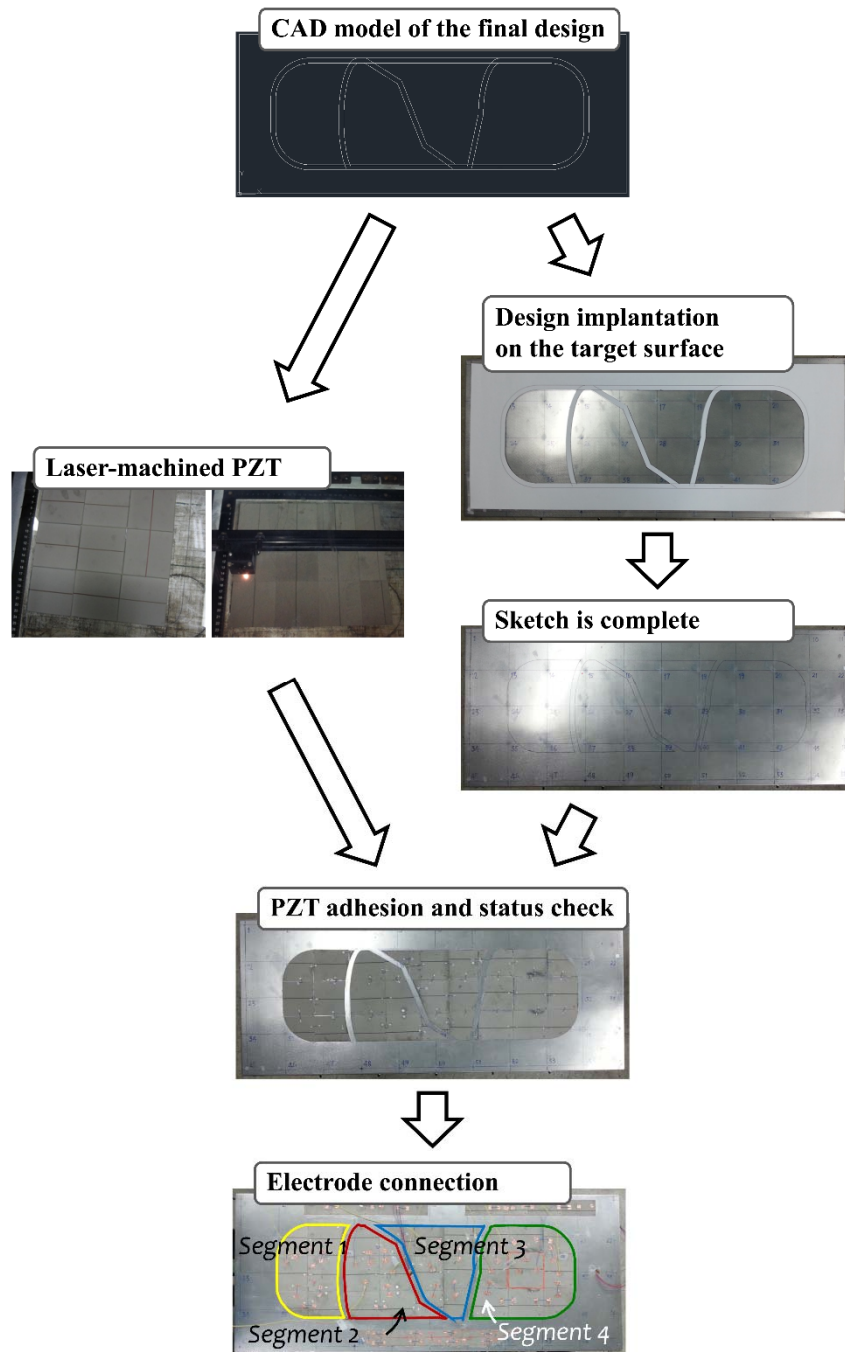
Fig. 3.1 Proposed fabrication process of the direct-type PEH skin design.

36

3.3 Experimental validation of the direct-type PEH skin

The concept of a smart plant has been developed for optimal process, risk, and asset managements. This requires monitoring of many process, risk, and logistics parameters by using advanced sensor technologies. It is thus expected to use wireless sensors extensively for remote and multi-purpose monitoring. However, one of the major concerns to use wireless sensors is a sustainable power source. In this work, the proposed direct-type PEH skin is intended to as a sustainable power source to the wireless sensor network.

The objective of this section is to validate the effectiveness of the proposed experimental method in designing the PEH skin. The validation was done in four steps: (a) comparison of in-plane normal strain values on a strain inflection line with those on a non-inflection line, (b) examination of the voltage cancellation effect between PEH skin segments divided by strain inflection lines, (c) power measurement and its rectification to obtain maximum output power form the PEH skin segments, and (d) operation of a wireless sensor network using the power output of the direct-type PEH skin.

3.3.1 Validation 1: Strain inflection line

To validate the strain inflection lines, two strain gauges are attached at different locations; one on a strain inflection line and the other on a non-inflection line. As shown in Figure 3.2, strain gauge #1 is located on the middle of 2nd strain inflection line, which is near the center of the top plate. Though this location is turned out to be a strain inflection line, it is actually a location where the largest out-of-plane deflection is existent (see Figure 2.6(b)). Therefore, it is meaningful to measure actual in-plane strain of this location and compare with its counterpart, to show that the out-of-plane deflection magnitude and strain inflection line location are not directly related. As the counterpart of strain gauge #1, strain gauge #2 is located outside the 1st strain inflection line. Unlike the strain gauge #1 location, this location experiences much smaller out-of-plane defection. The measured in-plane normal strains in the x - and y -directions are tabulated in Table 3.1. The value of S_{sum} on the inflection line was identified to be far smaller than that on the non-inflection line. So, it is valid to say that the strain inflection line is well selected with the negligibly small value of S_{sum} .
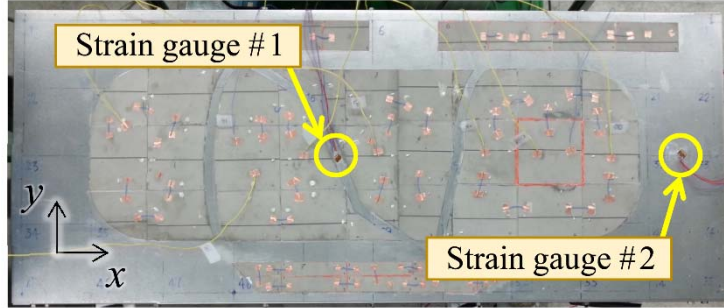
Fig. 3.2 Location of two strain gauges to validate the strain inflection lines of the proposed direct-type PEH skin design.

Table 3.1 Measured strain values from two strain gauges shown in Figure 3.2.

	Strain gauge #1 (on inflection)	Strain gauge #2 (NOT on inflection)
x-dir	7	9
y-dir	6	75

(unit: $\mu\varepsilon$)

3.3.2 Validation 2: Voltage cancellation effect

The voltage cancellation effect was examined by observing the output voltage phase of the PEH skin segments divided by the 1st and 2nd strain inflection lines in the time domain, as shown in Figure 3.3(a) and (b), respectively. On the left graph of Figure 3.3(a), the solid red and dotted blue curves indicate experimentally obtained voltages from two PEH skin segments divided by the 1st strain inflection line. Here, the blue colored PEH segment is optionally added to the target surface only to examine the voltage cancellation effect, not for vibration energy harvesting usage. It is apparent that the voltage signals tend to be out-of-phase although the two PEH segments are not in comparable size (see the dashed line box in Figure 3.3(a)). The voltage cancellation effect becomes more clear when two PEH skin segments are electrically connected to form $V_{red} + V_{blue}$. In this way, top electrodes of the two PEH skin segments share the equipotential surface, and therefore the voltage cancellation is deliberately induced. For comparison, the voltage subtraction is mathematically performed to yield $V_{red} - V_{blue}$. The dotted black curve is the resultant voltage of $V_{red} + V_{blue}$ (see the right hand side of Figure 3.3(a)), and the solid green curve is the resultant voltage of $V_{red} - V_{blue}$. The green curve generates higher peak-to-peak value of output voltage, which are also tabulated in Table 3.2. By applying this 1st strain inflection line, the red and blue PEH skin segments recorded 28.14 and 47.90 % voltage enhancement respectively, compared to the voltage cancellation situation. It can be concluded that, when designing a PEH skin, consideration of the voltage cancellation effect helps increase its power output.

For PEH skin segments divided by the 2nd strain inflection line, the observations made above become more apparent. Two PEH skin segments on the left side of the 2nd strain inflection line (the segment 1 and 2, as indicated in Figure 3.1) are grouped to form the red segment, and the segment 3 and 4 are grouped to form the blue segment (see the left hand side of Figure 3.3(b)). In this way, the two PEH skin segments can occupy comparable area, while divided by the 2nd strain inflection line. The solid red and dotted blue voltage curves obtained from two PZT segments are clearly out-of-phase from each other. Also, the voltage cancellation effect becomes more clear when $V_{red} + V_{blue}$ and $V_{red} - V_{blue}$ are compared. The peak-to-peak voltage results can be found in Table 3.2. By applying the 2nd strain inflection line, the output voltage of red and blue PEH skin segments are enhanced by 71.85 and 90.34 %, respectively, compared to the voltage cancellation situation. From these observations, it is concluded that the proposed direct-type PEH skin is well segmented across the inflection lines.

Table 3.2 The peak-to-peak voltage values from Figure 3.3 validating the voltage cancellation effect.

	V_{red}	V_{blue}	$V_{red} + V_{blue}$	$V_{red} - V_{blue}$
1st inflection	4.28	4.94	3.34	5.16
2nd inflection	4.09	4.53	2.38	5.50

(unit: V_{pp})

41
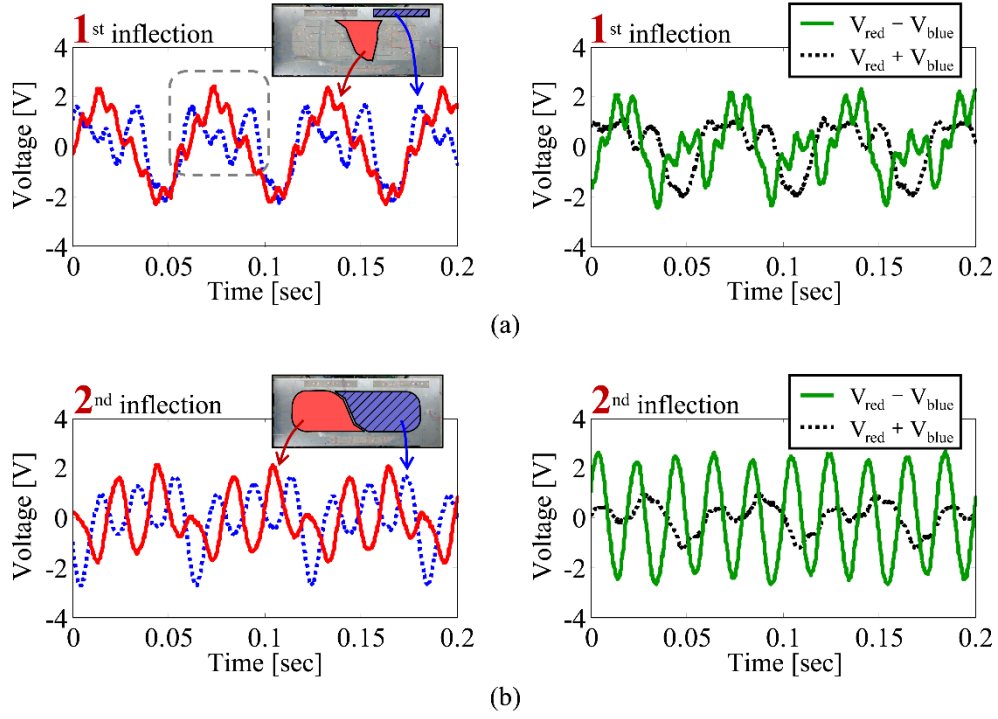
Fig. 3.3 Validation study and its result for the voltage cancellation effect – Voltage phase of the direct-type PEH segments divided by (a) 1st inflection line and (b) 2nd inflection line.

3.3.3 Validation 3: Output power and its rectified results

The output power of PEH skin segments are obtained by measuring applied voltage at a series of external load resistance. The well-known electrical power equation written below is applied to calculate power for each resistance value, and the maximum power output is found for each four PEH segments.

$$P = \frac{V^2}{R_L} \tag{3.1}$$

In general, it is very difficult to find optimal resistance values for all four PEH skin segments at the same time, due to electro-mechanical coupling nature of the PZT. That is, the change in external resistance value of one PEH segment affects mechanical characteristics of the whole system, altering optimal resistance value of neighboring PEH skin segments. So, in this work, the PEH skin segments other than the voltage measuring segment are maintained to be in open circuit state, assuming that the generated power from the other PEH skin segments are not in use. The output power results from each four PEH skin segments are depicted in Figure 3.4. Using the peak-to-peak voltage results, maximum power of 12.82, 14.85, 11.66, and 18.05 mW were obtained from four PEH skin segments, respectively. These results are tabulated in Table 3.3, along with measured voltage and the corresponding resistance value. The four PEH skin segments were verified to generate very large output power from vibration of the outdoor condensing unit's top plate.

In many practical situations, it is more worth using a rectified output rather than an alternating output power of a PEH. Therefore, two rectifier circuits shown in Figure 3.5 are used to rectify output voltage of the PEH skin segments. The schematic shown
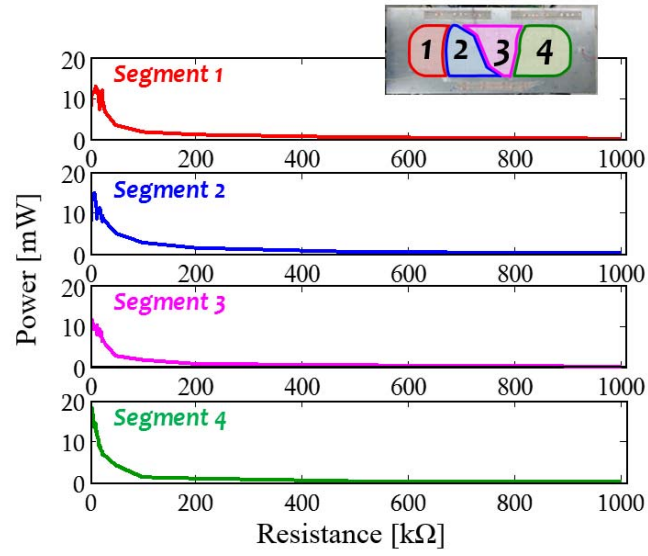
Fig. 3.4 Measured output power of the direct-type PEH skin segments with respect to external load resistance.

Table 3.3 The maximum output power results from each four PEH skin segment and its corresponding voltage and external load resistance values.

	Max. power [mW]	Voltage [V_{pp}]	Resistance [$k\Omega$]
Segment 1	12.82	11.88	11
Segment 2	14.85	12.19	10
Segment 3	11.66	4.563	5
Segment 4	18.05	9.500	5

44

in Figure 3.5(a) is a circuit to rectify the output voltage from each four PEH skin segments. Among four PEH skin segments, output power of the segment 1 and 4 are selected to be rectified for further comparison. The electrical state of PEH skin segments other than the voltage measuring PEH segment were maintained to be in open circuit state, as mentioned above. Also, the rectified voltages from all four PEH skin segments are electrically summed to obtain single output having a larger capacity. The schematic of rectifier circuit used for this purpose is shown in Figure 3.5(b). The four PEH skin segments are inevitably connected in parallel. Since the PZT sheets are bonded to the target surface by using the conductive epoxy, the four PEH skin segments inherently share the bottom electrode. So, the series connection between PEH segments were impossible to implement, which might have resulted in higher voltage output.

The obtained output power results are shown in Figure 3.6(a) and (b). Two different methods are used to obtain and compare the output power results. First, the peak-to-peak voltage measured at a series of resistance is used to obtain the result shown in Figure 3.6(a). This method will be named to be Case 1. The maximum output power values were 0.851, 1.31, and 0.825 mW from segment 1, segment 4, and sum of all four segments, respectively. These results are tabulated in Table 3.4, along with the corresponding resistance value. Compared with the maximum output power values listed in Table 3.3, significant decrease of values can be observed. This decrease is due to the rectification process, which is carried out by using a bridge diode. Also, note that the output power from parallelly connected four PEH skin segments is smaller than the power obtained from a single PEH segment (i.e., the segment 1 and 4). This is due to the voltage cancellation effect, which is still existent after the

45

rectification. Although all the voltage signals are converted to positive polarity after the rectification, the inextricable phase difference of the output voltage signals from each PEH skin segments resulted in this voltage reduction, behaving similar to the voltage cancellation effect.
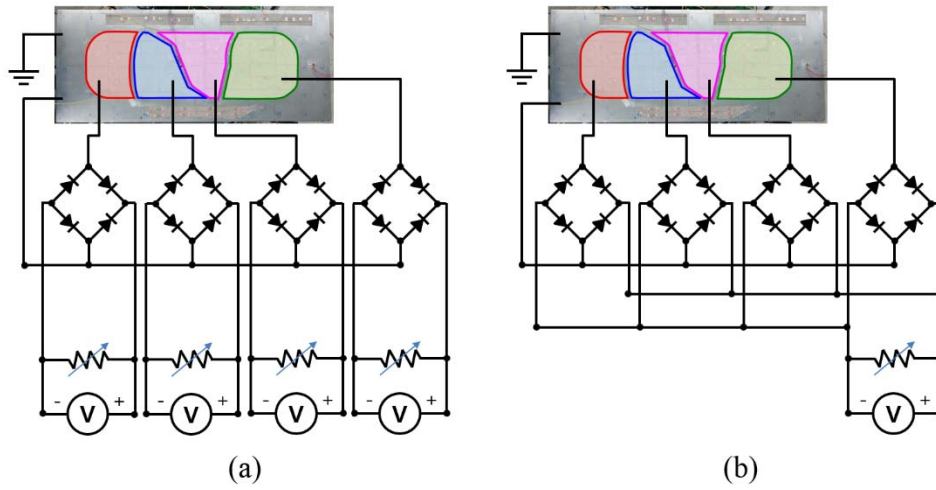
Fig. 3.5 Schematic of two rectifier circuit for the direct-type PEH skin, (a) rectified output power from each PEH skin segments and (b) parallelly summed output power rectified from all four PEH skin segments.

(a)

(b)
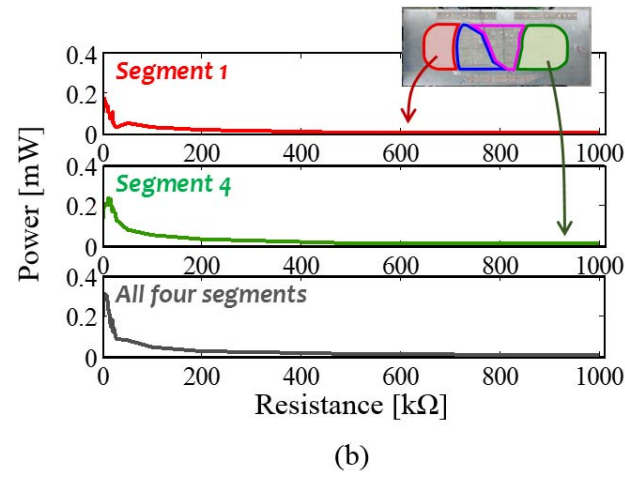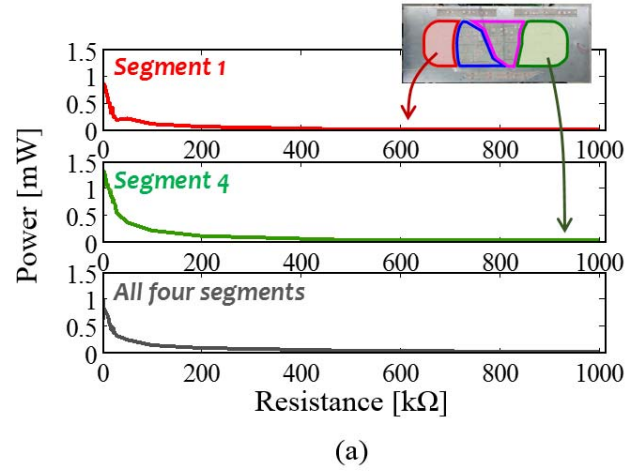
Fig. 3.6 Validation study and its result for the summation of rectified power output
– Measured output power of the direct-type PEH segments by using (a) the
peak-to-peak voltage (Case 1) and (b) the root-mean-squared voltage value
(Case 2).

47

Table 3.4 The maximum rectified output power results of the direct-type PEH skin segments by using two different methods (calculated from (i) Case 1: peak-to-peak voltage and (ii) Case 2: root-mean-squared voltage).

	Case 1		Case 2	
	Max power [mW]	Resistance [kΩ]	Max power [mW]	Resistance [kΩ]
Segment 1	0.851	5	0.173	5
Segment 4	1.31	5	0.235	12
All four segments	0.825	5	0.310	5

For Case 2, the root-mean-squared voltage values are used to calculate output power of the PEH skin segments. Figure 3.6(b) shows the output power result of Case 2, with respect to the external load resistance change. The maximum output power values were 0.173, 0.235, and 0.310 mW from segment 1, segment 4, and sum of all four segments, respectively. Here, the four PEH skin segments are also connected in parallel to obtain the power sum. These results are also tabulated in Table 3.4, along with the corresponding resistance values. By using the root-mean-squared voltage values, note that the output power from parallelly connected four PEH skin segments exceeds the power obtained from a single PEH segment. By parallelly adding the rectified voltage signals from each four PEH skin segments, voltage peaks of one signal can fill the voltage valleys of other signals, due to the phase difference between output voltage signals from each PEH segments. Therefore, while the maximum peak

48

value is reduced by voltage valleys of other signals, the overall average value can be improved. Here, the parallelly summed output power was observed to be enhanced by at least 31.9 % compared to the power obtained from segment 4, which was the largest among the four PEH skin segments.

3.3.4 Validation 4: Self-powered operation of a wireless sensor network

For the final verification of the proposed direct-type PEH skin design, five wireless sensors (AmbioSystems, LLC.) were employed. The specifications of the wireless sensors used in this verification is tabulated in Table 3.5 [77]. Each sensor was connected to the wireless platform (AmbioSystems, LLC., AmbioMote24) of which the operating input voltage is informed to be between 5 to 80 V. To determine the lower limit of the operating voltage, a simple experiment was conducted using a function generator (Agilent, 33220A) and the sensor was found to operate at over 2.3 V_{rms}.

The experimental setup to check sensor powering capability of the fabricate direct-type PEH skin is shown in Figure 3.7(a). Four three-dimensional acceleration sensors and one analog temperature sensor were connected to the PEH skin and the wireless platforms were used to transmit sensor signals to a laptop computer. In addition, two receivers, each of which is connected to a different laptop, were used because one receiver could treat up to four sensor signals. So, the real-time signal from two acceleration sensors (ID: 19 and 41) were carried by a wireless platform

(AmbioMote24-A), and two acceleration sensors and one temperature sensor (ID: 48, 52, and 40) were connected to the other platform (AmbioMote24-B). When the outdoor condensing unit was in operation and each output power from the arbitrarily chosen four PEH skin segments was provided, it was observed that all five sensor signals were successfully transmitted to two laptops. The screenshots of two laptops are shown in Figure 3.7(b). The sensor signal from the temperature sensor is highlighted with the orange solid lined box, while the blue dashed line boxes indicate the acceleration sensor signals. All five wireless sensor signals were successfully transmitted in real-time, proving that the fabricated PEH skin can supply sufficient power to operate the wireless sensor network.

An oscilloscope (LeCroy, LT354M) was also used to observe the output voltage in real-time. The output voltage signals from the four PEH skin segments are shown in Figure 3.8(a) and their Fourier transformed pairs are shown in Figure 3.8(b). The five wireless sensors being connected to the PEH skin, output voltage from each PEH skin segment was measured as $4 \sim 5$ V_{pp} . Four frequency peaks in Figure 3.8(b) and the ODS results in Figure 2.6 also confirms the consistency of the experiments.

Table 3.5 Specifications of wireless sensors provided by manufacturer.

	Model	Image	Specifications
Acceleration sensor	SENS-00003		・Range: ±3g ・Sensitivity: 300 mV/g (Accuracy: ±10 %) ・Number of axes: 3 ・Supply Current (max): 0.18 mA
Temperature sensor	SENS-00001		・Need lower energy in comparison with digital sensors.
Wireless platforms	AmbioMote24-A AmbioMote24-B		・Freq. band: 2.4 GHz ・Raw data rate: 2 Mbps (500 kbps pure data) ・Input voltage: 5~80 V ・Unique ID for each sensor ・80 m open air transmission range

(a)

(b)
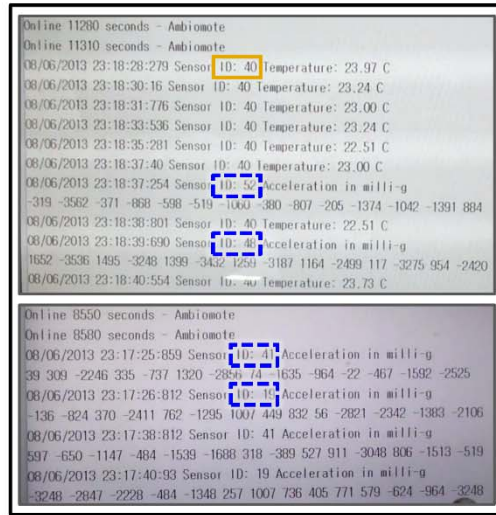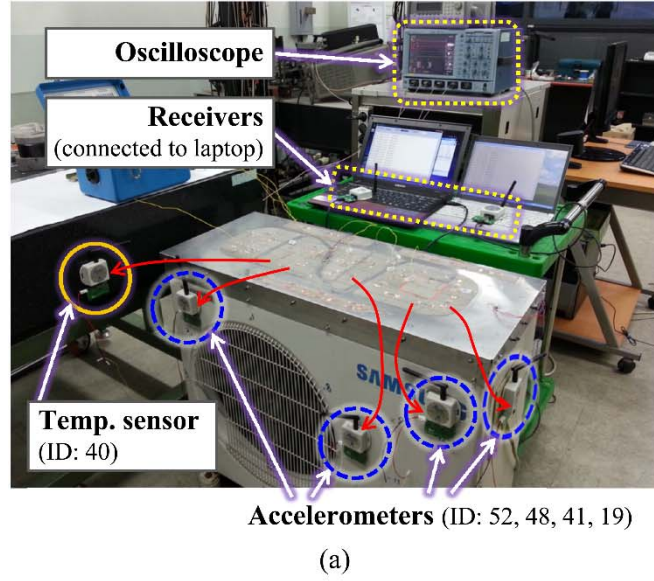
Fig. 3.7 (a) Experimental setup for a self-powered operation of a wireless sensor network (four accelerometers and one temperature sensor) through its integration to the direct-type PEH skin and (b) real-time monitored sensory data from self-powered wireless sensor network.
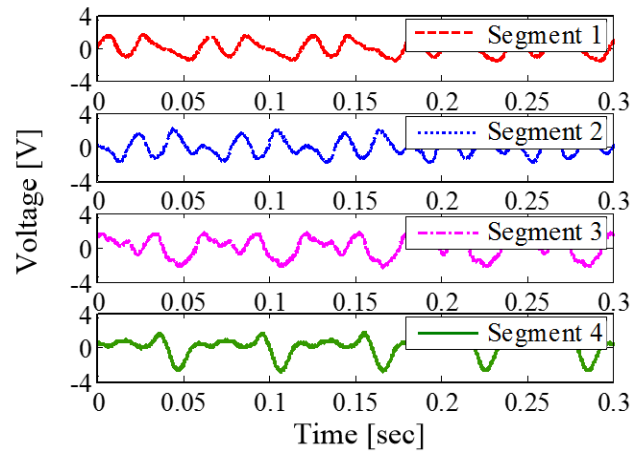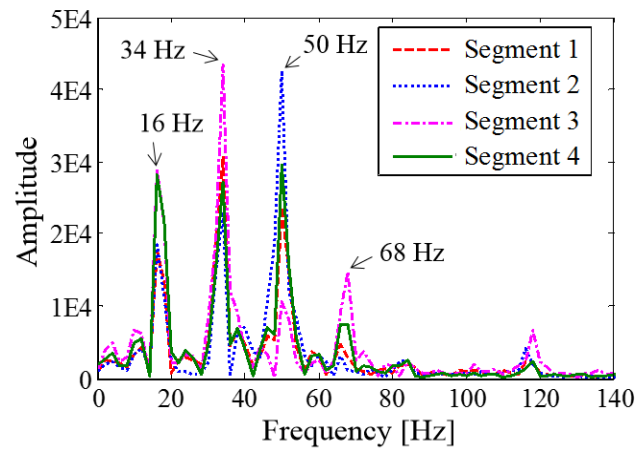
Fig. 3.8 (a) Output voltage histories harvested from four PEH skin segments and (b) the fast Fourier transformed result of the voltage signals.

Chapter 4

Add-on type PEH skin design and its experimental validation

4.1 Chapter overview

In this chapter, an add-on type PEH skin is proposed. For an actual mechanical system with plenty of vibration, it is sometimes impossible to apply the direct-type PEH skin, because of no presence of appropriate surface. Two different situations can be envisioned. First, the shape of the surface could be non-flat. Application of the proposed direct-type PEH skin on this non-flat surface is very difficult mainly due to the very stiff nature of the PZT. This problem seems to be easily solved by substituting the PZT with a piezoelectric material having flexibility, such as PVDF (PolyVvinyliDene Fluoride) or MFC (Macro-Fiber Composite). Here, instead of substituting the piezoelectric material, another solution is pursued to utilize the high energy conversion efficiency of the PZT. Second, not enough in-plane normal strain could be present, although considerable out-of-plane vibration is observed. The surface area could be too small, or the structure might be too stiff to have any shape

deflection. To harvest vibration energy from these situations, an add-on type PEH skin is devised as an alternative.

The PZT is attached on a flat substrate of the add-on type PEH skin, which is clamped to the target mechanical system with minimum spacing. Compared with the cantilevered PEH, the add-on type PEH skin can utilize larger area and be more stably fixed to the target surface by multiple clamping structure. Especially if the target mechanical system is vibrating at very low frequency, it is undesirable to apply a cantilever type PEH, since the vibration mode of a long cantilever might be interfered by touching the target surface. Moreover, unlike the direct-type PEH skin, finite element analysis can be easily applied to design the add-on type PEH skin, since the boundary conditions are simple and easy to predict. Therefore, ANSYS simulation (ANSYS, Inc.) is conducted to design the add-on type PEH skin by: (a) tuning the resonance frequency of the PEH skin unit to the actual vibrating frequency of the target surface and (b) optimizing the size of PEH skin segments to generate maximum electric power from given vibration condition. Here, the ODS of target surface is utilized to characterize actual excitation frequency and magnitude. Then, the add-on type PEH skin is fabricated as designed. The effectiveness of the add-on type PEH skin composed of three PEH segments is validated using several experiments.

4.2 Design of add-on type PEH skin based on ODS

As mentioned, there exists a situation where the above proposed direct-type PEH skin cannot be applied. Since the PZT patches of direct-type PEH skin are directly attached to the target surface, proper condition of the mechanical system can be limited. The limitation is mainly due to existence of curvature and/or not enough presence of in-plane normal strain on target surface. Although a considerable out-of-plane vibration is observed on the target surface, the PEH skin could not generate sufficient power because of not enough area. Also, if the structure is too stiff to have any shape deflection, very small in-plane normal strain is present, and therefore resulting in insufficient power generation.

In this work, an add-on type PEH skin is proposed as an alternative of the direct-type PEH skin, to harvest vibration energy from these situations. Basically, the PZT is attached on a flat substrate of the add-on type PEH skin, which is clamped to the target mechanical system with minimum spacing. Since the add-on type PEH skin cannot occupy a large area compared with the direct-type PEH skin, the output power might be insufficient. So, the add-on type PEH skin is designed to utilize resonance effect to amplify incoming vibration energy. For an add-on type PEH, one can easily recall a cantilevered PEH. Compared with the cantilever type PEH, the add-on type PEH skin can utilize larger area, and more stably fixed to the target surface especially when the incoming vibration is characterized in very low frequency range. Also, since the boundary conditions of the add-on type PEH skin are simple and easy to predict compared with the direct-type PEH skin, finite element analysis is applied to design the add-on type PEH skin. Designing by using the finite element analysis, the experimentally measured ODS of target surface is utilized to extract actual excitation

frequency and magnitude, which are used to characterize the incoming vibration to the add-on type PEH skin unit.

4.2.1 Target selection and vibration characterization.

The previously selected outdoor condensing unit is reexamined to inspect existence of appropriate location to apply the add-on type PEH skin. Among several surfaces of outdoor condensing unit, the side post shown in Figure 4.1(a) seemed to have suitable condition, and therefore it is intensively examined. This side post is a very rigid structure to support top plate of the outdoor condensing unit. So, although plenty of out-of-plane vibration is observed on this structure, existence of enough in-plane normal strain cannot be guaranteed. Moreover, the surface area of the side post is too small to apply the direct-type PEH skin. For these reasons, the side post is selected as an appropriate target surface for the add-on type PEH skin application.

The vibration characteristics of the side post is examined. Ten grid locations are selected along the center of the side post to have 50 mm uniform intervals, as shown in Figure 4.1(a). From these grid locations, an accelerometer (Brüel & Kjær, Type 4394) was used to measure vibration level of the target surface. The fast Fourier transformed result of measured vibration at a grid location is shown in Figure 4.2(b). Similar to the result shown in Chapter 2, the side post was vibrating in harmonics of the driving frequency induced by the cooling fan rotation (i.e., the harmonics of 16.5 Hz). Although the excitation frequencies were identical, maximum vibration level
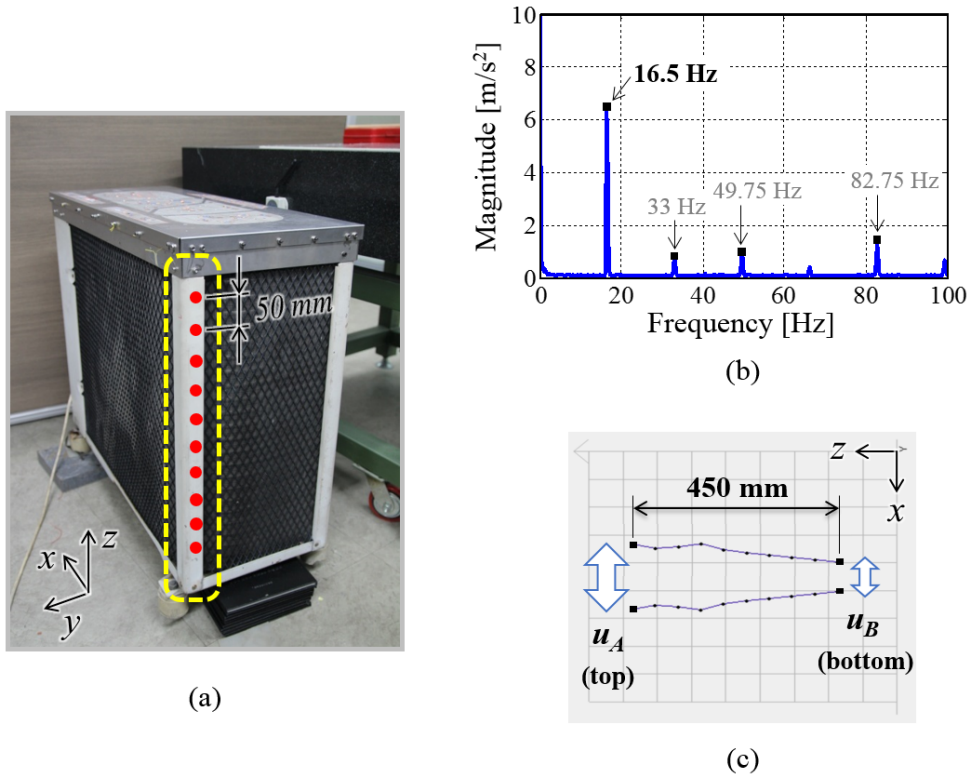
Fig. 4.1 Side post of the outdoor condensing unit, which is chosen as the target surface to apply the add-on type PEH skin: (a) Ten locations to examine vibration characteristics, (b) the fast Fourier transformed result to identify excitation frequency and vibration level, and (c) the ODS result of the target surface at 16.5 Hz.

was shown in different frequency. Here, the maximum vibration level was observed at 16.5 Hz, where relatively very low level of vibration could be found on the top plate of the outdoor condensing unit (see Figure 2.6(a)). Now, the ODS of the side post is measured. Two accelerometers were used, one as a reference located below the lowest grid location, and the other accelerometer was moved along the grid locations to measure acceleration of the target surface in out-of-plane direction. Along with these two accelerometers, a dynamic signal analyzer (Agilent, 35670A) was used to process the measured data from each ten grid locations into three data forms of APS (Auto Power Spectrum), CPS (Cross Power Spectrum), and FRF (Frequency Response Function). Post processing these data by using STAR Modal (Spectral Dynamics, Inc.) software, the ODS of the target surface can be successfully obtained. Figure 4.1(c) shows the ODS of the side post at 16.5 Hz, which is the frequency having the highest vibration level. Near the 16.5 Hz frequency band, the side post was identified to move in rigid body motion, instead of having any significant shape deflection. This rigid body motion was harmonic in x-direction, with displacement of the bottom grid point (indicated as u_B) being about 2.5 times smaller than that of the top grid point (i.e., u_A). The relative displacement data of the grid points will be considered in the finite element analysis aided design of the add-on type PEH skin in the following section.

59

4.2.2 Finite element analysis aided design optimization.

The finite element analysis is conducted to design the add-on type PEH skin. Regarding the long and narrow shape of the target surface, basic outline of the add-on type PEH skin design is decided to be in a long and narrow shape having two clamping structures. Based on this outline, the modal analysis is conducted using ANSYS to find appropriate dimensions of the add-on type PEH skin, to have fundamental resonance frequency tuned to the frequency of incoming vibration (i.e., 16.5 Hz) [78]. The schematic of the add-on type PEH skin is shown in Figure 4.2(a) and (b). Aluminum plate with 0.5 mm thickness and 35 mm width was selected as a substrate, fixed at both end to the clamping structures. Both the substrate and clamping structure are modeled with SOLID5 elements having three degrees of freedom (i.e., ux, uy, and uz). Also, the 0.27 mm thick PZT is uniformly attached on the aluminum substrate, and modeled with SOLID5 elements to have four degrees of freedom (i.e., ux, uy, uz, and volt). This SOLID5 element is a 3-D coupled-field solid element, which has 3-D magnetic, thermal, electric, piezoelectric, and structural field capability with limited coupling between the fields. In this work, the SOLID5 element is used in structural and piezoelectric analysis, since it has large deflection and stress stiffening capabilities.

First, the modal analysis is conducted using the PEH skin unit structure without any PZT segmentation, as schematically shown in Figure 4.2(a). All the node points of PZT elements on top and bottom surfaces of the PZT layer are set to compose equipotential surface, respectively. Two electric state of the PZT layer (i.e., short circuit and open circuit state) are considered in this analysis. The short circuit condition of the PEH skin unit is realized by fixing the electric state of the top and

60

(unit: mm)

(a)

(b)
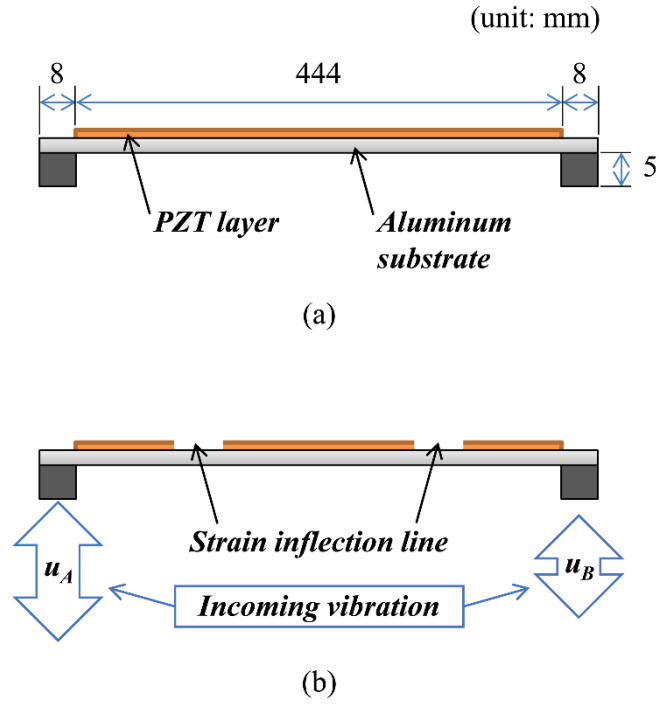
Fig. 4.2 Schematic of the proposed add-on type PEH skin: (a) The PZT layer uniformly attached to the aluminum substrate without any segmentation and (b) segmented PZT with respect to the incoming vibrations having different magnitude and/or phase (i.e., u_A and u_B).

Table 4.1 The lowest three resonance frequencies of the add-on type PEH skin, depicted in Figure 4.2(a) and (b).

	No segmentation		Segmented PZT	
	Short circuit	Open circuit	Short circuit	Open circuit
f_1	15.58	15.58	15.80	16.54
f_2	42.93	42.93	41.68	42.37
f_3	84.20	84.21	80.54	81.78

(unit: Hz)

bottom surface of the PZT layer in a ground state (i.e., volt = 0). For the open circuit condition, the bottom surface of the PZT layer is fixed in the ground state, while the electric condition of the top surface is remained in equipotential state without any additional definition. The fundamental resonance frequency of the add-on type PEH skin was found to be 15.58 Hz. The lowest three resonance frequency results are tabulated on the left hand side of Table 4.1. Without the PZT segmentation, the short circuit and open circuit resonance frequencies of the add-on type PEH skin did not differ from each other, which is due to the voltage cancellation effect (see Figure 4.3(b)). Here, since the resonance frequency of the add-on type PEH skin is more interested after the PZT segmentation, harmonic analysis is conducted to separate the PZT layer (i.e., locate the strain inflection lines) [78], and then redo the modal analysis to find short circuit and open circuit resonance frequencies.

62
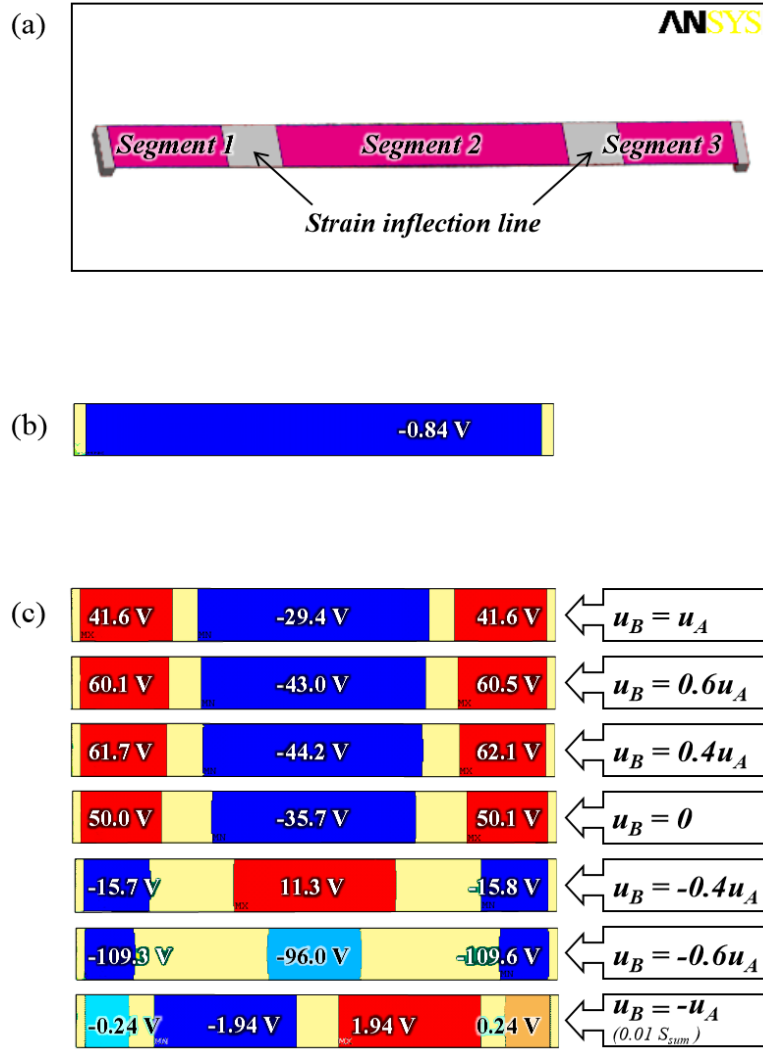
Fig. 4.3 (a) The finite element model of the add-on type PEH skin and (b) its open circuit voltage results without PEH skin segmentation, proving existence of voltage cancellation. (c) Different PEH skin segmentation results according to different combination of two incoming vibrations.

63

The harmonic analysis starts with the same structure shown in Figure 4.2(a). Two different vibration source are induced at each base of the clamping structure. Here, the ratio of these two vibration magnitude is chosen to be $u_A : u_B$ = 1:0.4, regarding the ODS of the target surface, obtained in the above section. While harmonically excited at 16.5 Hz, the strain inflection line was searched within range of $|S_{sum}| \leq 1 \times 10^{-5}$. After locating the strain inflection line, the PZT elements on the strain inflection line are deleted as schematically shown in Figure 4.2(b). The finite element analysis model of this schematic diagram is also depicted in Figure 4.3(a). To exclude these PZT elements for further analysis, a special option of "Ename = 0" is used on PZT elements, which are identified to be located on the strain inflection lines. By using this special option, the selected elements can be ignored during solution without actually removing the element from the model. Now, the modal analysis is conducted again using the PEH skin unit with segmented PZT layer. The resonance frequencies of segmented add-on type PEH skin are tabulated on the right hand side of Table 4.1. Since the voltage cancellation is prevented by the PZT segmentation, the difference between the short circuit and open circuit resonance frequencies are now obvious. Also, note that the fundamental open circuit resonance frequency of the add-on type PEH skin unit is tuned to the excitation frequency of the incoming vibration.

Now, the dimensions of the add-on type PEH skin is decided. Based on this dimensions, open circuit voltage of the add-on type PEH skin is analyzed regarding various possible combination of incoming vibration. The relative magnitude and phase of two incoming vibrations are changed to inspect for all possible vibrating situations. The PEH skin segmentation results according to different combination of incoming vibrations are shown in Figure 4.3(c). Here, the magnitude and phase of

64

incoming vibration on the left side (i.e., u_A) of the add-on type PEH skin was fixed, while the magnitude and phase of incoming vibration on the right side (i.e., u_B) was varied from $u_B = u_A$ (same magnitude and phase) to $u_B = -u_A$ (same magnitude with opposite phase). Here, the red and orange areas are showing positive electric potential state and blue and light blue areas are in negative potential state, while the yellow areas indicate the ground state ($V_{out} = 0$). The strain inflection line of these results were located to have in-plane normal strain value within range of $|S_{sum}| \leq 1 \times 10^{-5}$, except the $u_B = -u_A$ case (the strain inflection line of $u_B = -u_A$ case could be found below the in-plane normal strain range of $|S_{sum}| \leq 1 \times 10^{-7}$). For most of incoming vibration combinations, the add-on type PEH skin was observed to possess three PEH skin segments. Also, although the size of PEH segment differed according to different combination of two incoming vibrations, the center locations of the strain inflection lines were detected to have not much movement, especially when the two incoming vibrations were in-phase.

The proposed add-on type PEH skin is well segmented regarding the experimentally obtained ODS information, and successfully tuned to resonate at the frequency of incoming vibration. By the way, from analysis conducted above, the range of $|S_{sum}|$ to locate the strain inflection lines were arbitrarily chosen. To clarify this ambiguity, the open circuit voltage of the add-on type PEH skin is analyzed with respect to the $|S_{sum}|$ value as shown in Figure 4.4(a). The blue line indicates simulated open circuit voltage from segment 2, and red and magenta lines are the voltage outputs from segment 1 and 3, respectively. The red and magenta lines showed almost same voltage values, since the size of two PEH segments were almost the same. The strain

65

inflection lines were identified to be existent only within the in-plane normal strain range between $|S_{sum}| \leq 4 \times 10^{-7}$ and $|S_{sum}| \leq 3 \times 10^{-5}$. Within this in-plane strain range, two voltage peaks were observed at $|S_{sum}| \leq 8 \times 10^{-6}$ and $|S_{sum}| \leq 1.7 \times 10^{-5}$. Although the selected in-plane strain ranges were different, and therefore the size of PEH skin segments were different, these two design cases showed similar output voltage values. Exact dimensions of these two design cases are shown in Figure 4.4(b). Since these two optimized design cases show similar output voltage, the $|S_{sum}| \leq 1.7 \times 10^{-5}$ case having smaller PEH skin segment is chosen as the final design of the proposed add-on type PEH skin, considering economic efficiency.

(a)

(b)
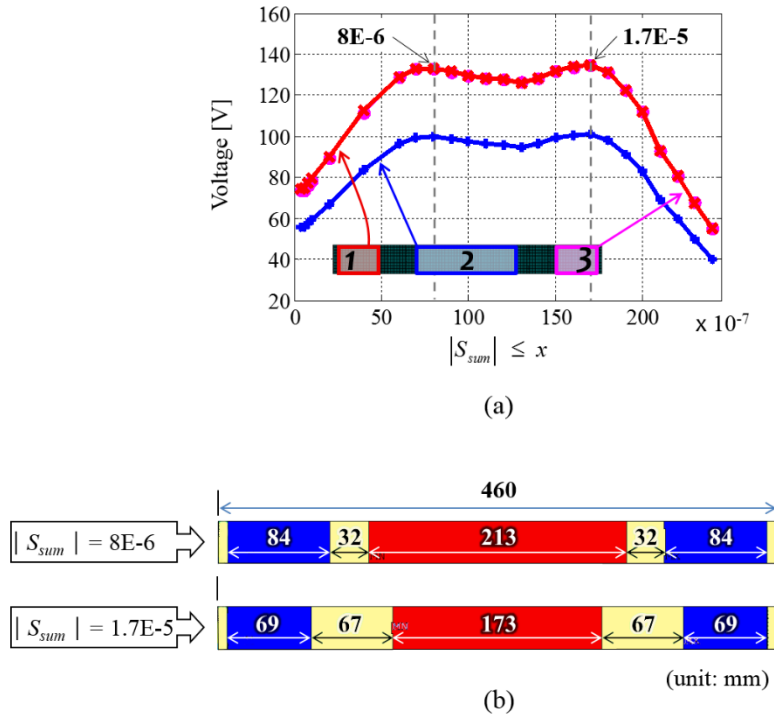
Fig. 4.4 (a) Open circuit voltage results from three PEH segments of the add-on type PEH skin, with respect to selected $\left|S_{sum}\right|$ range. (b) Two optimized design results of the add-on type PEH skin having maximum output voltage.

4.3 Experimental validation of the add-on type PEH skin

The previously selected optimized design of the add-on type PEH skin is fabricated as shown in Figure 4.5(a). The PSI-5H4E piezoceramic sheets (Piezo Systems, Inc.) are selected as the piezoelectric material, and an automatic dicing saw (DISCO Corporation, DAD3350) is used to cut PZT sheets as designed. Unlike the PEH skin segments of the direct-type PEH skin design, the three PEH segments of the add-on type PEH skin are in rectangular shape without any curved edges. Therefore, the automatic dicing saw is used instead of the CNC laser cutter, since a more precise and fast processing is possible by using the dicing saw. Also, a two-part epoxy adhesive (3M, Scotch-Weld DP-460) is used instead of the conductive epoxy (ITW Chemtronics, CW-2400). Although the DP-460 epoxy is not an electrically conductive material, it is discovered by some experiments that the voltage measurement of a PEH is not interfered if the thickness of the epoxy layer between the PZT and substrate is kept below 30 μm. Compared with the use of conductive epoxy, fabrication of a PEH by using the DP-460 epoxy is much comfortable. This is mainly due to following two reasons: (a) it is much easier to evenly spread the DP-460 epoxy on the substrate surface, because of the very low density and longer worklife compared with the conductive epoxy and (b) it is much safer in situations having overflowed epoxy, because it does not cause electrically short state between the top and bottom electrodes of the PEH skin segments. The full cure of DP-460 epoxy requires 48 hours at room temperature (i.e., at 22 °C) [79]. In this work, an electric oven (UNOX S.p.A., XF006) is used to cure the epoxy used to fabricate the add-on type PEH skin. Heated at 80 °C, curing process of the DP-460 epoxy could be accelerated and finished within an hour.

68

The fabricated add-on type PEH skin is installed at the target surface of outdoor condensing unit as shown in Figure 4.5(b). Then, the effectiveness of this add-on type PEH skin is experimentally validated. Since a very thin aluminum plate is chosen as the flat substrate of this add-on type PEH skin, it was very difficult to apply strain gauges directly on the strain inflection line. Also, the add-on type PEH skin unit does not have any bare surface without PZT, which is discovered as a non-strain inflection line. So, a counterpart of strain gauge on the strain inflection line has no appropriate surface to be located. For these reasons, the validation of strain inflection line by using the strain gauges is omitted for the add-on type PEH skin case. Instead, effectiveness of the strain inflection line is verified by demonstrating the voltage cancellation effect and comparing the output power results from each PEH skin segments.

(a)

(b)
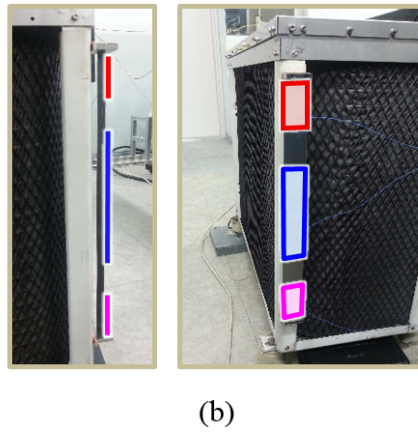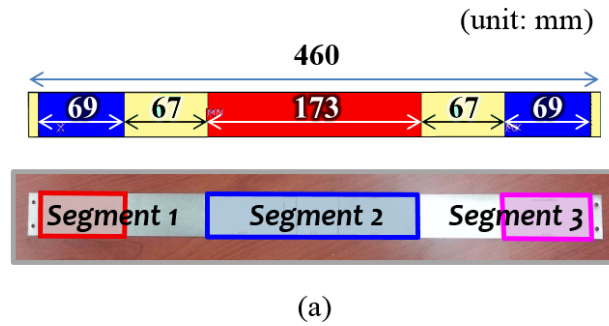
Fig. 4.5 (a) The dimensions of selected optimized add-on type PEH skin design, and its fabricated result having three PEH skin segments. (b) The add-on type PEH skin installed at the target surface of outdoor condensing unit (the three PEH skin segments are highlighted for better visibility).

4.3.1 Validation 1: Voltage cancellation effect

The voltage cancellation effect was examined by observing the output voltage phases of the three PEH skin segments divided by the strain inflection lines in the time domain, as shown in Figure 4.6. For each PEH segment, the open circuit voltage is measured by connecting the top and bottom electrodes directly to an oscilloscope (LeCroy, LT354M). Since the internal impedance of the oscilloscope is set to be 1 MΩ, directly measured voltage from a PEH segment can be regarded as open circuit voltage. Three output voltage signals measured from the PEH skin segments are shown in Figure 4.6(a), with respect to the time domain. Unlike the voltage signals of direct-type PEH skin segments, the voltage signals of the add-on type PEH skin segments are in simple sinusoidal shape. This signal shapes are mainly due to utilization of resonance phenomenon, in designing the add-on type PEH skin. Also, an obvious phase difference between the three signal can be observed. The output voltage signal of segment 1 and 3 were in phase, while the voltage measured from segment 2 showed out of phase alone. This phase difference is consistent with the simulation result identified above, where the output voltage value of segment 2 in the middle showed different sign compared with the other two output voltages from segment 1 and 3 (see Figure 4.3(c)).

For more clear validation of voltage cancellation effect, the three PEH skin segments are electrically connected to form $V_{red} + V_{blue} + V_{magenta}$. In this way, all three PEH skin segments can share the top electrodes to form a equipotential surface, and therefore the voltage cancellation is deliberately induced. For comparison, the voltage subtraction is mathematically performed to yield $V_{blue} - V_{red}$. These two resultant

71
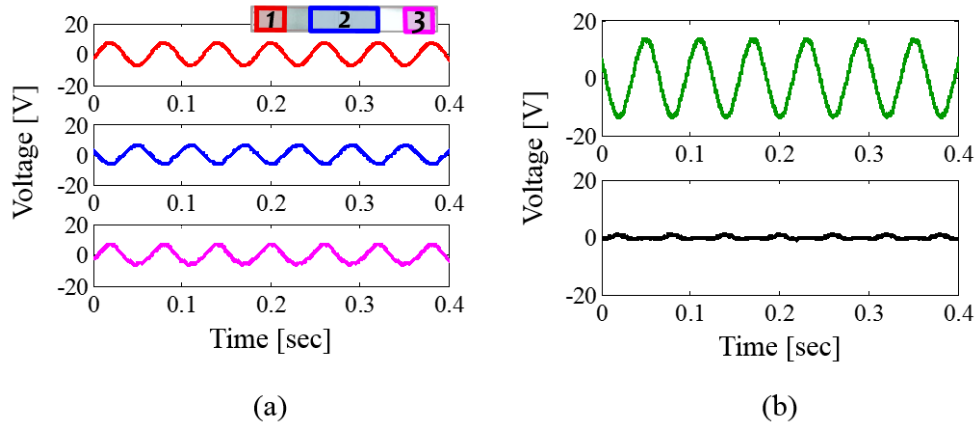
Fig. 4.6 Validation study and its result for the voltage cancellation effect – (a) The output voltage signals measured from the three PEH skin segments of the add-on type PEH skin. (b) The voltage cancellation effect demonstrated by using the three PEH skin segments.

Table 4.2 The peak-to-peak voltage values from Figure 4.6 validating the voltage cancellation effect.

V_{red}	V_{blue}	$V_{magenta}$	$V_{red} + V_{blue} + V_{magenta}$	$V_{blue} - V_{red}$
15.63	12.81	13.91	2.63	27.97

(unit: V_{pp})

72

voltage signals are shown in Figure 4.6(b). The black curve is the resultant voltage of $V_{red} + V_{blue} + V_{magenta}$ and the green curve indicates the resultant voltage of $V_{blue} - V_{red}$. Although the $V_{magneta}$ is not involved to mathematically calculate the green curve, the peak-to-peak value of this resultant voltage was distinctively higher than the others. The peak-to-peak voltage results are tabulated in Table 4.2. By applying the strain inflection lines, the voltage enhancement of the three PEH skin segments were 494.3, 387.1, and 428.9 %, for red, blue, and magenta segments, respectively, compared to the voltage cancellation situation. These enhancement levels are surprisingly high, since the voltage cancellation effect of the add-on type PEH skin was very intense. According to this observation, it is concluded that the proposed add-on type PEH skin is well segmented across the inflection lines.

4.3.2 Validation 2: Output power and its rectified results

The output power of add-on type PEH skin segments are obtained by measuring applied voltage at a series of external load resistance, in the same way as in Chapter 3. Using the measured voltage values from each three PEH skin segment, the output voltage is calculated by Equation (3.1). Here, since the add-on type PEH skin is composed of multiple PEH segments, it is also very difficult to find optimal resistance values for all three PEH skin segments at the same time, due to electro-mechanical

coupling nature of the PZT. Therefore, the PEH skin segments other than the voltage measuring segment are maintained to be in open circuit state, assuming that the generated power from the other PEH skin segments are not in use. The output power results from each three PEH skin segments are shown in Figure 4.7. Using the measured peak-to-peak voltage values, maximum power of 3.53, 1.88, and 1.98 mW were obtained from three PEH skin segments, respectively. These results are also tabulated in Table 4.3, along with measured voltage and the corresponding resistance value. Although the peak-to-peak output voltage values measured from PEH segments of the add-on type PEH skin are analogous to those from direct-type PEH skin segments, the output power values are calculated to be much smaller due to larger corresponding external load resistance value.

Now, two rectifier circuits shown in Figure 4.8 are used to rectify output voltage of the PEH skin segments. The schematic shown in Figure 4.8(a) is a circuit to rectify the output voltage from each three PEH skin. While measuring the rectified output voltage of a selected PEH skin segment, the other two PEH segments were maintained to be in open circuit state, as in the measurement process above. Also, the rectified voltages from all three PEH skin segments are electrically summed to obtain single output having a larger capacity. The schematic of rectifier circuit used for this purpose is shown in Figure 4.8(b). Similar to the direct-type PEH skin, the three PEH skin segments of the add-on type PEH skin are inevitably connected in parallel, since the bottom electrodes of all PZT sheets are bonded to the substrate structure of the add-on type PEH skin. So, the series connection between PEH segments were impossible to implement, which might have resulted in higher voltage output.

74
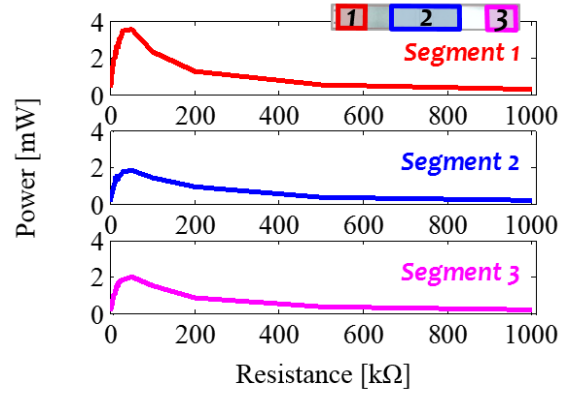
Fig. 4.7 Measured output power of the add-on type PEH skin segments with respect to external load resistance.

Table 4.3 The maximum output power results from each three PEH skin segment and its corresponding voltage and external load resistance values.

	Max. power [mW]	Voltage [V_{pp}]	Resistance [kΩ]
Segment 1	3.53	13.3	50
Segment 2	1.88	9.69	50
Segment 3	1.98	9.94	50

75

The obtained rectified output power results are shown in Figure 4.9, with respect to the external load resistance change. For the rectified power of individual PEH segment, the result measured from segment 1 and 2 are selected as a representative among the three PEH segments. The root-mean-squared voltage values are used to calculate output power of the PEH skin segments. The maximum output power values were 0.115, 0.099, and 0.258 mW from segment 1, segment 2, and sum of all three segments, respectively. These results are also tabulated in Table 4.4, along with the corresponding resistance values. Compared with the rectified output power results of the direct-type PEH skin, the rectified output power values of the add-on type PEH skin seem quite competitive (see Table 3.4). Although the measured output power of the add-on type PEH skin without the rectification showed relatively very small values, the competitive values of the rectified power are thought to be mainly due to simple sinusoidal shape of the output voltage signal. Here, the parallelly summed output power was observed to be enhanced by 124.3 and 160.6 % compared to the power obtained from segment 1 and 2, respectively. According to this observation, effectiveness of the add-on type PEH skin was verified and a significant power could be generated especially when the output is rectified.
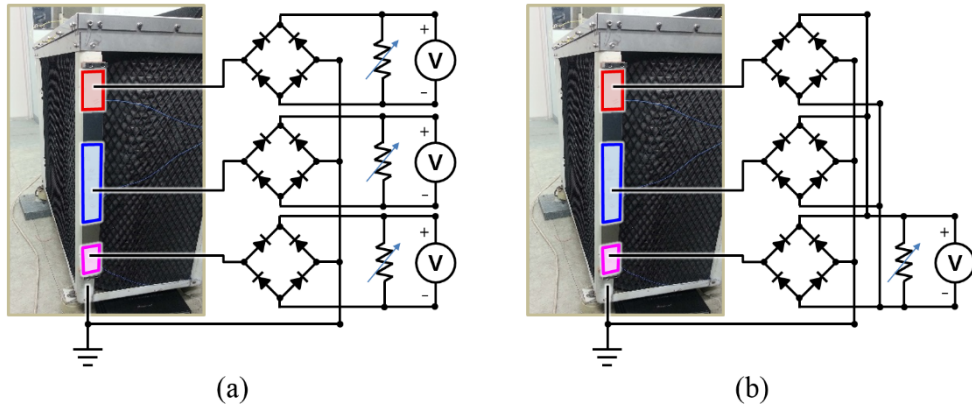
Fig. 4.8 Schematic of two rectifier circuit for the add-on type PEH skin, (a) rectified output power from each PEH skin segment and (b) parallelly summed output power rectified from all three PEH skin segments.
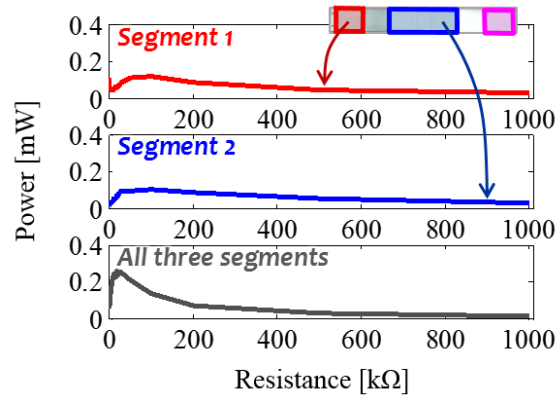
Fig. 4.9 Validation study and its result for the rectified power output of the add-on type PEH skin, calculated by using the root-mean-squared voltage values.

Table 4.4 The maximum rectified output power results of the add-on type PEH skin segments calculated by using the root-mean-squared voltage values.

	Max power [mW]	Resistance [kΩ]
Segment 1	0.115	100
Segment 2	0.099	100
All three segments	0.258	20

78

Chapter 5

Conclusions

This work proposes two practical methods to design the PEH skin based on experimentally measured ODSs. Depending on shape condition of the vibrating target surface, one can choose a type of the PEH skin to apply: (i) the direct-type PEH skin for a flat and large surface application and (ii) the add-on type PEH skin for a non-flat and/or small surface application, where not enough in-plane strain is existent. This classification of the PEH skin regarding the shape of the target surface is mainly due to the utilization of PZT as the piezoelectric material. Although the energy conversion efficiency of PZT is very high, the extremely brittle nature has limited its application to a flat surface only. The design and fabrication process of the two PEH skin types are introduced and their effectiveness is experimentally validated.

For the direct-type PEH skin, the PZT patches are designed to be directly attached to the target surface. Directly applied onto a flat and large surface, the direct-type PEH skin is very compact and does not require any extra space above the vibrating target surface. The key step of ODS based direct-type PEH skin design is to extract continuous in-plane normal strain values from measured out-of-plane deformations

of the target mechanical system, which are generally discrete. To replicate the actual deflection shape of the target surface, a polynomial curve fitting is applied to obtain continuous out-of-plane deflection data from the discrete ODS measurement data. Then, continuous in-plane normal strain values are calculated to locate strain inflection lines. For final design of the direct-type PEH skin, multiple strain inflection lines found at specific excitation frequencies are used to enhance its energy harvesting capability. The proposed design procedure was applied to design a direct-type PEH skin for an outdoor condensing unit's top plate. Compared with an analytical method, this design method is advantageous since it is free from unacknowledged modeling errors, and therefore readily applicable to engineering facilities having complex boundary conditions. The fabrication process was proposed and the performance of the direct-type PEH skin was experimentally validated. The validation was conducted in four steps. First, the in-plane normal strain values on a strain inflection line were measured and compared with those on a non-inflection line. The value of S_{sum} on the inflection line was turned out to be far smaller than that on the non-inflection line, verifying the location of strain inflection line. Second, apparent voltage cancellation effect was examined between PEH skin segments divided by strain inflection lines, proving that the direct-type PEH skin is well segmented across the inflection lines. Third, the output power of the PEH skin segments are measured along with their rectified values. Calculated from the root-mean-squared voltage values, the electrically summed output power was enhanced compared to output power from a single PEH segment. Finally, the fabricated direct-type PEH skin is applied to operate a wireless sensor network, which is the most common but a still challenging application of the energy harvesting. The PEH skin could supply enough power to operate the wireless sensor network consisting of five wireless sensors.

For the add-on type PEH skin, the PZT is attached on a flat substrate, which is clamped to the target mechanical system with minimum spacing. Compared with the cantilevered PEH, the add-on type PEH skin can utilize larger area and be more stably fixed to the target surface by multiple clamping structure. On the other hand, the add-on type PEH skin cannot occupy a large area compared with the direct-type PEH skin, which might result in insufficient output power. So, the add-on type PEH skin is designed to utilize resonance effect to amplify incoming vibration energy. Also, unlike the direct-type PEH skin, finite element analysis can be easily applied to design the add-on type PEH skin, since the boundary conditions are simple and easy to predict. Therefore, the ANSYS simulation is conducted to design and optimize the add-on type PEH skin. Here, the key step of add-on type PEH skin design is the utilization of ODS information to characterize incoming vibration to the simulated model. The proposed design procedure was applied to design an add-on type PEH skin for a side post of the outdoor condensing unit. The fabrication process was proposed and the performance of the add-on type PEH skin was experimentally validated in two steps. First, the voltage cancellation effect was demonstrated using the three PEH skin segments, proving that the add-on type PEH skin is well segmented across the inflection line. Second, the output power of the PEH skin segments are measured along with their rectified values, proving that a significant power could be generated especially when the output is rectified.

The proposed PEH skin designs are targeted to be readily applicable to existing engineering facilities with vibration. By applying the proposed design methods to an outdoor condensing unit, which is an example of small scale actual mechanical system, the practical aspect of the two PEH skin designs are experimentally verified.

81

Especially, The generated power from the fabricated PEH skin successfully operated a wireless sensor network, proving the effectiveness of the proposed PEH skin design. Applied to a larger plant facilities, the generated power from the PEH skin is expected to be supplied to various types of wireless sensors, which are utilized for risk management, asset management, and process management, and therefore contributing to realize a smart plant.

Appendix A

Harvestable vibration energy map

A.1 Appendix overview

In general, to avoid unwanted failures and/or accidents, a lot of sensors are in use to monitor plant facilities. Recently, as the wireless sensor technology has improved to require lower power, the energy harvesting has received much attention supplying power to these sensors. To realize a smart plant, various types of sensors are utilized for risk management, asset management, and process management, as schematically shown in Figure A.1. Since the ultimate goal of the energy harvesting is to successfully operate wireless sensors on actual plant facilities, this work analyzed the vibration energy level of a fan blower unit, which is a common facility in various plant sites. Also, the vibration energy level is reorganized to constitute a harvestable vibration energy map. Considering the shape and vibration energy level at the same time, it is expected to be very helpful deciding an appropriate type and location of an vibration energy harvester.
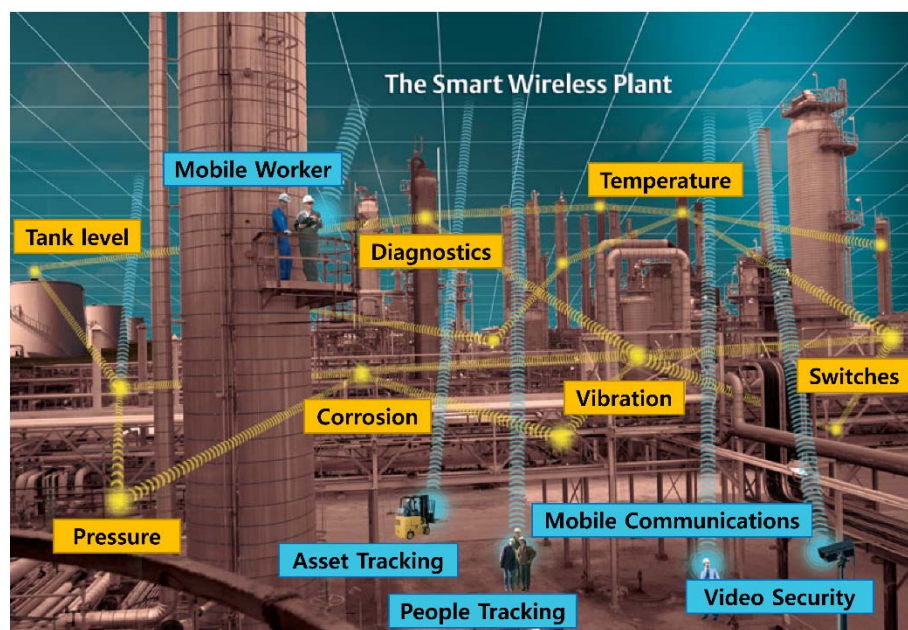
Fig. A.1 Schematic of a smart plant realized using various wireless sensors [80].

A.2 Target selection and vibration characterization

A target mechanical system is carefully selected based on following three criteria: (a) the mechanical system is required to have appropriate vibrating surface, (b) the facility should be at easily accessible location, and (c) the target is preferred to be a common facility which can be found in various plant sites. Four mechanical systems are considered as candidates, as shown in Figure A.2. All these candidates were found

(a) (b)

(c) (d)

Fig. A.2 Four candidates of target mechanical system in Seoul National University Gwanak Campus: (a) cooling water pumps in Building 301, (b) hydraulic pumps in Building 301, (c) a boiler unit in Building 313, and (d) a fan blower unit in Building 68 (i.e., the 1st power plant).

in building machine rooms of Seoul National University Gwanak Campus. Among the four candidates, the fan blower unit was selected to be the target mechanical system, since this facility possesses largest flat surfaces with plenty of vibration. Also, the fan blower unit is a very common facility in many plant sites, which is used to circulate cooling air to a larger facilities such as an industrial steam boiler.

While the fan blower unit is under operation, an accelerometer (Brüel & Kjær, Type 4394) with a dynamic signal analyzer (Agilent, 35670A) is used to collect vibration level data from various surface. Large vibration level was measured mainly at 38 and 450 Hz, which are originated from electromagnetic motor operation and cooling fan blade rotation, respectively. Figure A.3 shows the vibration characteristics of a drive belt housing. The drive belt being directly connected between the electromagnetic motor and the cooling fan rotor, the surfaces of the belt housing were vibrating at both 38 and 452 Hz. The vibration characteristics of the cooling fan blade housing are shown in Figure A.4. Due to the cooling fan rotation, the fan blade housing was mainly vibrated at 452 Hz, with a highest vibration level of maximum 7.2g (g = 9.8 m/s^2). Also, the vibration characteristics of the blast pipe was identified as shown in Figure A.5. Similar to the cooling fan blade housing, the blast pipe was vibrating mainly at 452 Hz. This is due to the air fluctuation flowing inside the blast pipe, generated by the cooling fan blade rotation.
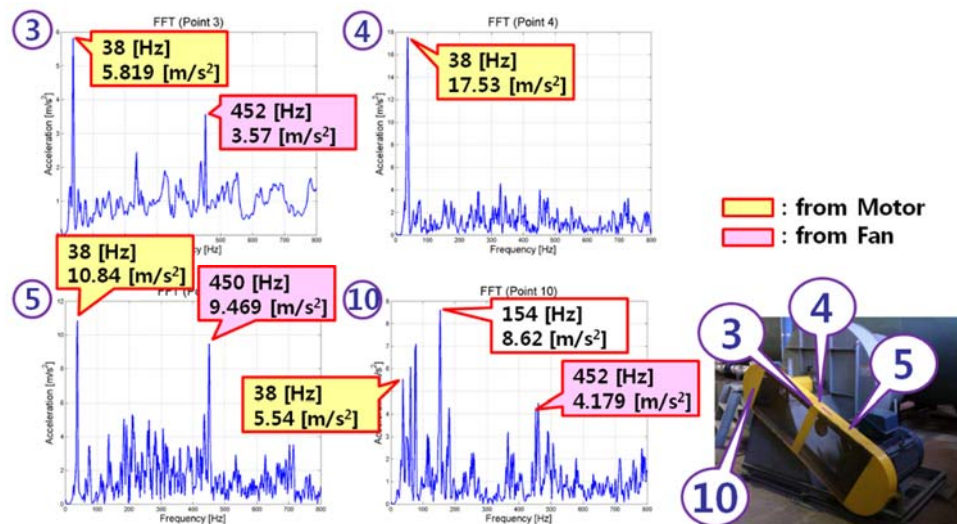
Fig. A.3 Identified vibration characteristics of the drive belt housing.

87
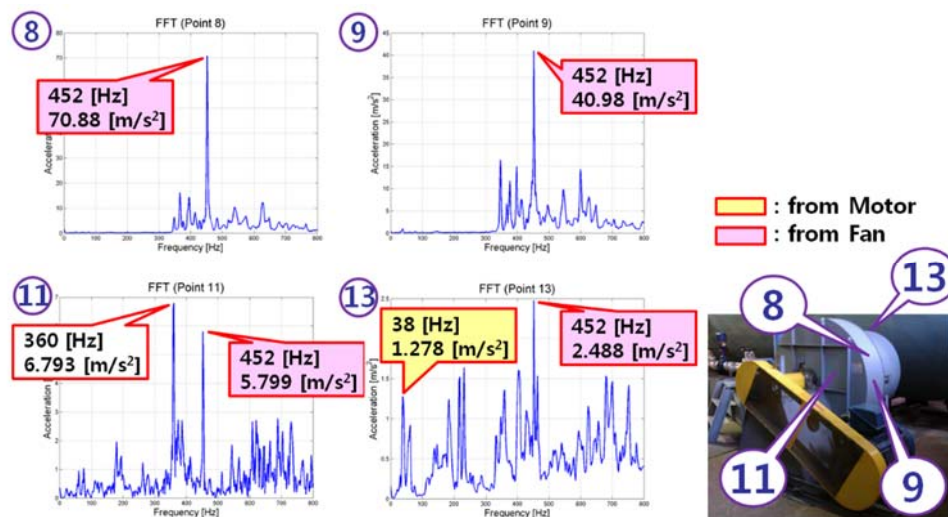
Fig. A.4 Identified vibration characteristics of the cooling fan blade housing.
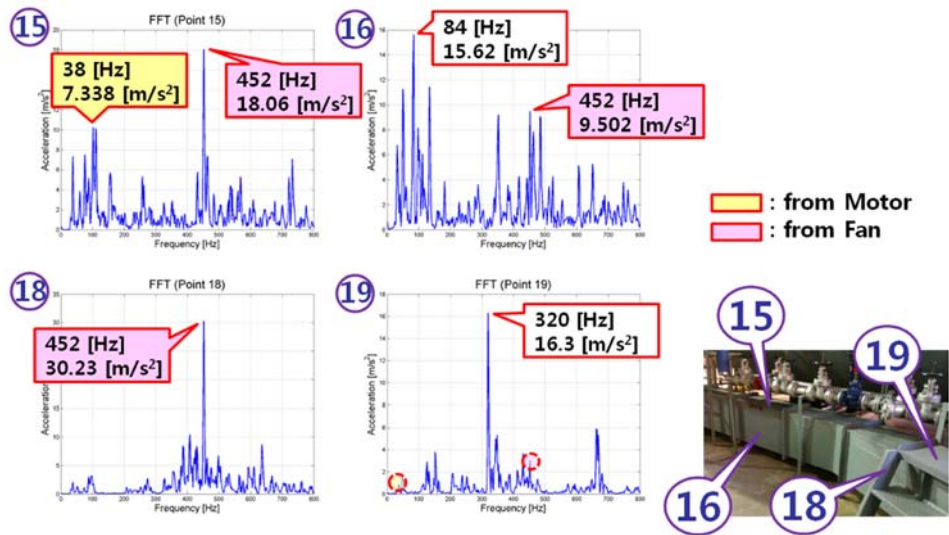
Fig. A.5 Identified vibration characteristics of the blast pipe.

A.3 Harvestable vibration energy map

The harvestable vibration energy map is constructed using vibration characteristics of the target mechanical system identified above. Based on the vibration levels, the surfaces of interest were divided into 6 sections as shown in Figure A.5. With the highest vibration level shown on a curved surface of the cooling fan blade housing, a large surface including the drive belt housing and the blast pipe showed acceleration around 2g level. By using this harvestable energy map, it will be very helpful to decide an appropriate type and location of an energy harvester, since the shape of surface and its vibration energy level can be considered at the same time.
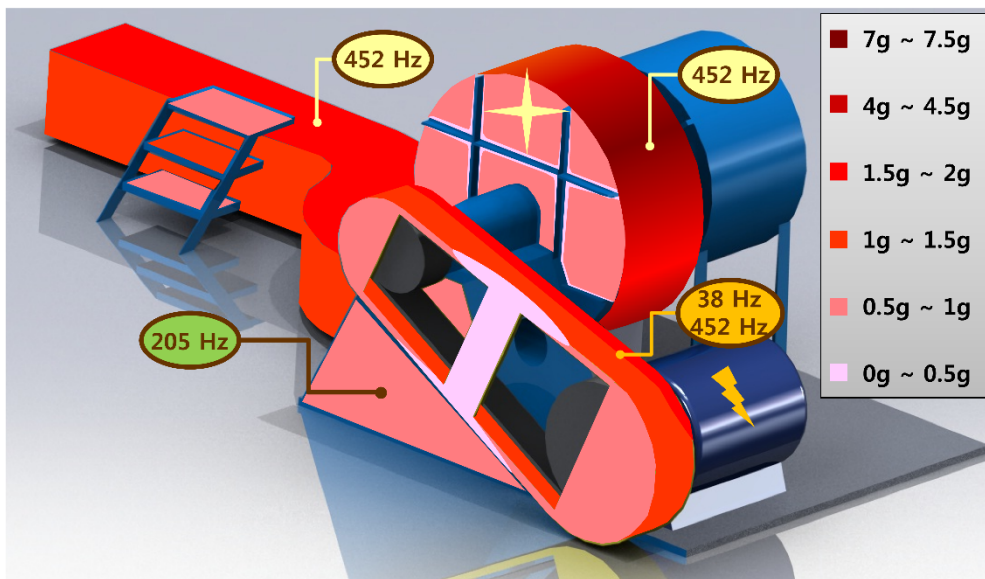
Fig. A.6 Harvestable vibration energy map.

90

Appendix B

Numerical data for PSI-5H4E piezoceramic

PZT-5H is the most commonly used engineering piezoceramic for a PEH fabrication. The PZT-5H piezoceramic sheet used in this work is PSI-5H4E, manufactured by Piezo Systems, Inc. The three-dimensional piezoelectric properties of PSI-5H4E is provided in Table B.1. In addition to these data, the mass density is reported as 7800 kg/m^3 [81]. The PSI-5H4E piezoceramic sheets are available in the standard 72.4 mm square size, and poled along the thickness direction. Also, three different thickness are provided as 0.127, 0.191, and 0.267 mm.

Table B.1 Three-dimensional piezoelectric properties of PSI-5H4E

Descriptions	Value	Units
s_{11}^E	16.1	pm^2/N
s_{12}^E	-4.84	pm^2/N
s_{13}^E	-6.00	pm^2/N
s_{33}^E	20.00	pm^2/N
s_{55}^E	52.00	pm^2/N
s_{66}^E	41.9	pm^2/N
d_{31}	-320	pm/V
d_{33}	650	pm/V
d_{15}	741	pm/V
$\varepsilon_{11}^T / \varepsilon_0$	3800	
$\varepsilon_{33}^T / \varepsilon_0$	3800	

According to the piezoelectric properties of PSI-5H4E provided in Table B.1, the elastic compliance matrix of the PZT sheet at constant electric field (poling direction is chosen to be the thickness direction) can be rewritten as:

$$\mathbf{s}^E = \begin{bmatrix} 1.61E-11 & -4.84E-12 & -6.00E-12 & 0 & 0 & 0 \\ -4.84E-12 & 1.61E-11 & -6.00E-12 & 0 & 0 & 0 \\ -6.00E-12 & -6.00E-12 & 2.00E-11 & 0 & 0 & 0 \\ 0 & 0 & 0 & 5.20E-11 & 0 & 0 \\ 0 & 0 & 0 & 0 & 5.20E-11 & 0 \\ 0 & 0 & 0 & 0 & 0 & 4.19E-11 \end{bmatrix}$$

(B.1)

Also, the piezoelectric matrix ($\mathbf{d}$) and the permittivity matrix at constant stress ($\boldsymbol{\varepsilon}^T$) are as follows:

$$\mathbf{d} = \begin{bmatrix} 0 & 0 & 0 & 0 & 7.41E-10 & 0 \\ 0 & 0 & 0 & 7.41E-10 & 0 & 0 \\ -3.20E-10 & -3.20E-10 & 6.50E-10 & 0 & 0 & 0 \end{bmatrix}$$ (B.2)

and

$$\boldsymbol{\varepsilon}^T = \begin{bmatrix} 3.36E-8 & 0 & 0 \\ 0 & 3.36E-8 & 0 \\ 0 & 0 & 3.36E-8 \end{bmatrix}$$

(B.3)

where the relative permittivity matrix at constant stress ($\boldsymbol{\varepsilon}_r^T$) is

$$\boldsymbol{\varepsilon}_r^T = \begin{bmatrix} 3800 & 0 & 0 \\ 0 & 3800 & 0 \\ 0 & 0 & 3800 \end{bmatrix}$$

(B.4)

93

References

[1]   S. R. Anton and H. A. Sodano, A review of power harvesting using piezoelectric materials (2003–2006), *Smart Materials and Structures* 16 (2007) R1-R21.

[2]   S. P. Beeby, M. J. Tudor, and N. M. White, Energy harvesting vibration sources for microsystems applications, *Measurement Science and Technology* 17 (2006) R175-R195.

[3]   K. A. Cook-Chennault, N. Thambi, and A. M. Sastry, Powering MEMS portable devices— a review of non-regenerative and regenerative power supply systems with special emphasis on piezoelectric energy harvesting systems, *Smart Materials and Structures* 17 (2008) 043001.

[4]   N. S. Hudak and G. G. Amatucci, Small-scale energy harvesting through thermoelectric, vibration, and radiofrequency power conversion, *Applied Physics Letters* 103 (2008) 101301.

[5]   S. Priya and D. J. Inman, *Energy Harvesting Technologies*, Springer, New York, NY, 2009.

94

[6]   S. Roundy and P. K. Wright, A piezoelectric vibration based generator for wireless electronics, *Smart Materials and Structures* 13 (2004) 1131-1142.

[7]   S. Roundy, P. K. Wright, and J. Rabaey, A study of low level vibrations as a power source for wireless sensor nodes, *Computer Communications* 26 (2003) 1131–1144.

[8]   P. Glynne-Jones and N. M. White, Self-powered systems: a review of energy sources, *Sensor Review* 21 (2001) 91-97.

[9]   G. Park, T. Rosing, M. D. Todd, C. R. Farrar, and W. Hodgkiss, Energy Harvesting for Structural Health Monitoring Sensor Networks, *Journal of Infrastructure Systems* 14 (2008) 64-79.

[10]   R. Torah, P. Glynne-Jones, M. Tudor, T. O'Donnell, S. Roy, and S Beeby, Self-powered autonomous wireless sensor node using vibration energy harvesting, *Measurement Science and Technology*, 19 (2008) 125202.

[11]   P. Glynne-Jones, M. J. Tudor, S. P. Beeby, and N. M. White, An electromagnetic, vibration-powered generator for intelligent sensor systems, *Sensors and Actuators A* 110 (2004) 344-349.

[12]   S. P. Beeby, R. N. Torah, M. J. Tudor, P. Glynne-Jones, T. O'Donnell, C. R. Saha, and S. Roy, A micro electromagnetic generator for vibration energy harvesting, *Journal of Micromechanics and Microengineering* 17 (2007) 1257-1265.

[13]   P. Wang, K. Tanaka, S. Sugiyama, X. Dai, X. Zhao, J. Liu, A micro electromagnetic low level vibration energy harvester based on MEMS technology, *Microsystem Technologies* 15 (2009) 941-951.

[14]   B. Yang, C. Lee, W. Xiang, J. Xie, J. H. He, R. K. Kotlanka, S. P. Low, and H. Feng, Electromagnetic energy harvesting from vibrations of multiple frequencies, *Journal of Micromechanics and Microengineering* 19 (2009) 035001.

[15]   P. D. Mitcheson, P. Miao, B. H. Stark, E. M. Yeatman, A. S. Holmes, and T. C. Green, MEMS electrostatic micropower generator for low frequency operation, *Sensors and Actuators A* 115 (2004) 523-529.

[16]   M. Lallart, S. Pruvost, and D. Guyomar, Electrostatic energy harvesting enhancement using variable equivalent permittivity, *Physics Letters A* 375 (2011) 3921-3924.

[17]   C. P. Le and E. Halvorsen, MEMS electrostatic energy harvesters with end-stop effects, *Journal of Micromechanics and Microengineering* 22 (2012) 074013.

[18]   G. -J. Sheu, S. -M. Yang, and T. Lee, Development of a low frequency electrostatic comb-drive energy harvester compatible to SoC design by CMOS process, *Sensors and Actuators A* 167 (2011) 70–76.

[19] J. Kymissis, C. Kendall, J. Paradiso, and N. Gershenfeld, Parasitic Power Harvesting in Shoes, *Second International Symposium on Wearable Computers* (1998) 132-139.

[20] Z. Wang and Y. Xu, Vibration energy harvesting device based on air-spaced piezoelectric cantilevers, *Applied Physics Letters* 90 (2007) 263512.

[21] J. E. Kim and Y. Y. Kim, Analysis of Piezoelectric Energy Harvesters of a Moderate Aspect Ratio With a Distributed Tip Mass, *Journal of Vibration and Acoustics* 133 (2011) 041010

[22] J. R. Liang and W. H. Liao, Piezoelectric Energy Harvesting and Dissipation on Structural Damping, *Journal of Intelligent Material Systems and Structures* 20 (2009) 515-527.

[23] L. Wang and F. G. Yuan, Energy harvesting by magnetostrictive material (MsM) for powering wireless sensors in SHM, *SPIE Smart Structures and Materials & NDE and Health Monitoring, 14th International Symposium* (2007) 1-11.

[24] L. Wang and F. G. Yuan, Vibration energy harvesting by magnetostrictive material, *Smart Materials and Structures* 17 (2008) 045009.

[25] J. Hu, F. Xu, A. Q. Huang, and F. G. Yuan, Optimal design of a vibration-based energy harvester using magnetostrictive material (MsM), *Smart Materials and Structures* 20 (2011) 015021.

97

[26] K. A. Cook-Chennault, N. Thambi, M. A. Bitetto, and E.B. Hameyie, Piezoelectric Energy Harvesting: A Green and Clean Alternative for Sustained Power Production, *Bulletin of Science, Technology & Society* 28 (2008) 496-509.

[27] A. Erturk and D. J. Inman, *Piezoelectric Energy Harvesting*, John Wiley & Sons, Ltd., Chichester, West Sussex, United Kingdom, 2011.

[28] S. Priya, Advances in energy harvesting using low profile piezoelectric transducers, *Journal of Electroceramics* 19 (2007) 165-182.

[29] H. A. Sodano, D. J. Inman, and G. Park, A Review of Power Harvesting from Vibration using Piezoelectric Materials, *The Shock and Vibration Digest* 36 (2004) 197-205.

[30] C. D. Richards, M. J. Anderson, D. F. Bahr, and R. F. Richards, Efficiency of energy conversion for devices containing a piezoelectric component, *Journal of Micromechanics and Microengineering* 14 (2004) 717-721.

[31] H. W. Kim, A. Batra, S. Priya, K. Uchino, D. Markey, R. E. Newnham, and H. F. Hofmann, Energy Harvesting Using a Piezoelectric "Cymbal" Transducer in Dynamic Environment, *Japanese Journal of Applied Physics* 43 (2004) 6178-6183.

[32] M. Ericka, D. Vasic, F. Costa, G. Poulin, and S. Tliba, Energy harvesting from vibration using a piezoelectric membrane, *Journal de Physique IV* 128 (2005) 187-193

[33]   S. Kim, W. W. Clark and Q. -M. Wang, Piezoelectric Energy Harvesting with a Clamped Circular Plate: Analysis, *Journal of Intelligent Material Systems and Structures* 16 (2005) 847-854.

[34]   S. Kim, W. W. Clark and Q. -M. Wang, Piezoelectric Energy Harvesting with a Clamped Circular Plate: Experimental Study, *Journal of Intelligent Material Systems and Structures* 16 (2005) 855-863.

[35]   S. Wang, K. H. Lam, C. L. Sun, K. W. Kwok, H. L. W. Chan, M. S. Guo, and X. -Z. Zhao, Energy harvesting with piezoelectric drum transducer, *Applied Physics Letters* 90 (2007) 113506.

[36]   A. Massaro, S. D. Guido, I. Ingrosso, R. Cingolani, M. D. V, M. Cori, A. Bertacchini, L. Larcher, and A. Passaseo, Freestanding piezoelectric rings for high efficiency energy harvesting at low frequency, *Applied Physics Letters* 98 (2011) 053502.

[37]   Z. Wang and Y. Xu, Vibration energy harvesting device based on air-spaced piezoelectric cantilevers, *Applied Physics Letters* 90 (2007) 263512.

[38]   A. Erturk, *Electromechanical Modeling of Piezoelectric Energy Harvesters*, Ph. D Thesis, Virginia Polytechnic Institute and State University, 2009.

[39]   A. Erturk and D. J. Inman, Issues in mathematical modeling of piezoelectric energy harvesters, *Smart Materials and Structures*, 17 (2008) 065016.

[40]   A. Erturk and D. J. Inman, A Distributed Parameter Electromechanical Model for Cantilevered Piezoelectric Energy Harvesters, *Journal of Vibration and Acoustics* 130 (2008) 041002.

[41]   A. Erturk and D. J. Inman, On Mechanical Modeling of Cantilevered Piezoelectric Vibration Energy Harvesters, *Journal of Intelligent Material Systems and Structures* 19 (2008) 1311-1325.

[42]   A. Erturk and D. J. Inman, An experimentally validated bimorph cantilever model for piezoelectric energy harvesting from base excitations, *Smart Materials and Structures*, 18 (2009) 025009.

[43]   N. E. duToit, B. L. Wardle, and S. Kim, Design Considerations for MEMS-Scale Piezoelectric Mechanical Vibration Energy Harvesters, *Integrated Ferroelectrics* 71 (2005) 121-160.

[44]   J. Ajitsaria, S. Y. Choe, D. Shen, and D. J. Kim, Modeling and Analysis of a Bimorph Piezoelectric Cantilever Beam for Voltage Generation, *Smart Materials and Structures* 16 (2007) 447-454.

[45]   F. Goldschmidtboeing and P. Woias, Characterization of different beam shapes for piezoelectric energy harvesting, *Journal of Micromechanics and Microengineering* 18 (2008) 104013.

[46]   S. Roundy, E. S. Leland, J. Baker, E. Carleton, E. Reilly, E. Lai, B. Otis, J. M. Rabaey, P. K. Wright and V. Sundararajan, Improving power output for

vibration-based energy scavengers *IEEE Pervasive Computing* 4 (2005) 28-36.

[47] B. Zheng, C. -J. Chang, and H. C. Gea, Topology optimization of energy harvesting devices using piezoelectric materials, *Structural and Multidisciplinary Optimization* 38 (2009) 17-23.

[48] C. J. Rupp, A. Evgrafov, K. Maute ,and M. L. Dunn, Design of Piezoelectric Energy Harvesting Systems: A Topology Optimization Approach Based on Multilayer Plates and Shells, *Journal of Intelligent Material Systems and Structures* 20 (2009) 1923-1939.

[49] N. G. Stephen, On energy harvesting from ambient vibration, *Journal of Sound and Vibration* 293 (2006) 409-425.

[50] Y. B. Jeon, R. Sood, J. H. Jeong, and S. Kim, MEMS Power Generator With Transverse Mode Thin Film PZT, *Sensors and Actuators A* 122 (2005) 16-22.

[51] H. -B. Fang, J. -Q. Liu, Z. -Y. Xu, L. Dong, D. Chen, B. -C. Cai, and Y. Liu, A MEMS-Based Piezoelectric Power Generator for Low Frequency Vibration Energy Harvesting, *Chinese Physics Letters* 23 (2006) 732-734.

[52] H. A. Sodano, G. Park, and D. J. Inman, Estimation of Electric Charge Output for Piezoelectric Energy Harvesting, *Strain Journal* 40 (2004) 49-58.

[53] F. Lu, H. P. Lee, and S. P. Lim, Modeling and analysis of micro piezoelectric power generators for micro-electromechanical-systems applications, *Smart Materials and Structures* 13 (2004) 57-63.

[54] S. -N. Chen, G. -J. Wang, and M. -C. Chien, Analytical modeling of piezoelectric vibration-induced micro power generator, *Mechatronics* 16 (2006) 379-387.

[55] J. E. Kim, D. S. Kim, P. S. Ma, and Y. Y. Kim, Multi-physics interpolation for the topology optimization of piezoelectric systems, *Computer Methods in Applied Mechanics and Engineering* 199 (2010) 3153-3168.

[56] Y. Tadesse, S. Zhang, and S. Priya, Multimodal Energy Harvesting System: Piezoelectric and Electromagnetic, *Journal of Intelligent Material Systems and Structures* 20 (2009) 625-632.

[57] S. C. Stanton, C. C. McGehee, and B. P. Mann, Nonlinear dynamics for broadband energy harvesting: Investigation of a bistable piezoelectric inertial generator, *Physica D* 239 (2010) 640-653.

[58] A. Khaligh, P. Zeng, and C. Zheng, Kinetic Energy Harvesting Using Piezoelectric and Electromagnetic Technologies—State of the Art, *IEEE Transactions on Industrial Electronics* 57 (2010) 850-860.

[59] M. Ferrari, V. Ferrari, M. Guizzetti, B. Andò, S. Baglio, and C. Trigona, Improved energy harvesting from wideband vibrations by nonlinear piezoelectric converters, *Sensors and Actuators A* 162 (2010) 425-431.

102

[60] M. Ferrari, V. Ferrari, M. Guizzetti, D. Marioli, and A. Taroni, Piezoelectric multifrequency energy converter for power harvesting in autonomous microsystems, *Sensors and Actuators A* 142 (2008) 329-335.

[61] J. E. Kim, J. C. Ryu, P. S. Ma, and Y. Y. Kim, *Energy harvester unit module, multi-axis energy harvester assembly made from the same, and multi-axis energy harvester multi-assembly made from the same*, Korean Patent No. 101067019, 2011.

[62] V. R. Challa, M. G. Prasad, Y. Shi, and F. T. Fisher, A vibration energy harvesting device with bidirectional resonance frequency tenability, *Smart Materials and Structures* 17 (2008) 015035.

[63] S. Lee and B. D. Youn, A design and experimental verification methodology for an energy harvester skin structure, *Smart Materials and Structures* 20 (2011) 057001.

[64] S. Lee and B. D. Youn, A new piezoelectric energy harvesting design concept: multimodal energy harvesting skin, *IEEE Transactions on Ultrasonics, Ferroelectrics, and Frequency Control* 58 (2011) 629-45.

[65] A. Erturk, P. A. Tarazaga, J. R. Farmer, and D. J. Inman, Effect of Strain Nodes and Electrode Configuration on Piezoelectric Energy Harvesting From Cantilevered Beams, *Journal of Vibration and Acoustics* 131 (2009) 011010.

[66] S. Lee , B. D. Youn, and B. C. Jung, Robust segment-type energy harvester and its application to a wireless sensor, *Smart Materials and Structures* 18 (2009) 095021.

[67] B. J. Schwarz and M. H. Richardson, Experimental Modal Analysis, *CSI Reliability Week, Orlando, FL.* (1999).

[68] B. J. Schwarz and M. H. Richardson, Introduction to ODS, *CSI Reliability Week, Orlando, FL.* (1999).

[69] B. J. Schwarz and M. H. Richardson, Scaling Mode Shapes Obtained from Operating Data, *Sound and Vibration* 37 (2003) 18-22.

[70] M. Batel, Operational Modal Analysis – Another Way of Doing Modal Testing, *Sound and Vibration* 36 (2002) 22-27.

[71] A. B. Stanbridge, M. Martarelli, and D. J. Ewins, Measuring strain response mode shapes with a continuous-scan LDV, *Shock and Vibration* 9 (2002) 19-27.

[72] B. J. Schwarz and M. H. Richardson, Obtaining Stresses and Strains from ODS Data, *IMAC-XXI: Conference & Exposition on Structural Dynamics - Innovative Measurement Technologies* (2003).

[73] A. Erturk, Piezoelectric energy harvesting for civil infrastructure system applications: Moving loads and surface strain fluctuations. *Journal of Intelligent Material Systems and Structures* 22 (2011) 1959-1973.

[74]   *IEEE Standard on Piezoelectricity (IEEE Standard 176-1987)*, Institute of Electrical and Electronic Engineers, Inc., New York, NY, 1988.

[75]   S. H. Crandal, N. C. Dahl, T. J. Lardner, R. R. Archer, and N. H. Cook, *Introduction to the Mechanics of Solids: Second Edition with SI Units*, McGraw-Hill, Singapore, 1978.

[76]   D. J. Ewins, *Modal Testing: Theory, Practice and Application 2nd ed.* Research Studies Press Ltd., Baldock, Hertfordshire, England, 2000.

[77]   http://www.ambiosystems.com/ (Accessed 13 April 2014).

[78]   *ANSYS Structural Analysis Guide (Release 12.1)*, ANSYS Inc., Canonsburg, PA, 2009.

[79]   3M Scotch-Weld Epoxy Adhesives DP-460 Off-White / DP-420 Off-White (Technical Data), 3M, St. Paul, MN, 1997.

[80]   http://www2.emersonprocess.com/ (Accessed 13 April 2014).

[81]   Piezo Systems Catalog #8 (2011), Piezo Systems Inc., Woburn, MA, 2011.

Abstract (Korean)

분절된 스킨형 압전 에너지 수확장치

김 홍 진

서울대학교 대학원

기계항공공학부

본 논문에서는 각종 구동 주파수의 진동을 기반으로 효과적으로 작동이 가능한 스킨형 압전 에너지 수확장치를 제안한다. 스킨형 압전 에너지 수확장치의 설계에 해석적 모델을 활용했던 기존의 연구들과 달리, 본 논문에서는 대상 기계 시스템의 운전 중 변형 형상을 이용한 실험적 설계 기법을 제안한다. 이 설계 기법은 대상 기계 시스템의 실제 진동 특성을 스킨형 압전 에너지 수확장치의 설계에 효과적으로 반영할 수 있는 매우 실용적인 방법이다. 대상 기계 시스템의 실제 변형 형상을 설계에 반영하기 위해서, 면내 수직 변형률 값들을 대상 기계 시스템에서 이산 측정한 면외 방향 변형 정보로부터 보간을 통해 구하게 된다. 그 다음 변형률 기반의 변곡선을 구하기 위한 정보를 추출하여, 전압 상쇄를 방지할 수 있도록 하나 이상의 변형률 변곡선을 갖는 스킨형 압전 에너지 수확장치를 설계 하였다. 이러한 설계 기법을 검증하기 위해 실제 에어컨 실외기를 대상으로 네 개의 조각으로 구성된 스킨형 압전 에너지 수확장치를 제작하였으며, 무선 센서 네트워크를 성공적으로 구동할 수

있는 충분한 전력을 생산할 수 있음을 실험적으로 입증 하였다. 또한 스킨형 압전 에너지 수확장치의 분할 여부에 따른 검증 실험들을 통해 압전 소자의 적절한 분할이 더 큰 출력에 기여함을 확인할 수 있었다.

더불어 이러한 설계 기법의 확장으로써, 곡면의 형태이거나 면내 변형률이 작은 값을 갖는 등 까다로운 환경에 대해 적용이 가능한 "추가식" 스킨형 압전 에너지 수확장치를 제안한다. 추가식 스킨형 압전 에너지 수확장치의 경우, 대상 기계 시스템의 운전 중 변형 형상을 고려하되 유한 요소 해석을 이용해 변형률 변곡선의 위치를 결정하게 된다. 직접식 스킨형 압전 에너지 수확장치의 경우와 달리 구조가 간단해서 유한 요소 해석을 이용한 설계가 손쉬우면서도 정확하기 때문이다. 또한, 에너지 수확장치가 최대 출력 전력을 가질 수 있도록 압전 분절의 크기를 해석을 통해 결정 하였다. 이렇게 설계한 추가식 스킨형 압전 에너지 수확장치의 성능은 실험을 통해 검증 하였으며, 특히 출력을 정류 할 경우에 더 효과적임을 알 수 있었다.